

Anharmonicity in the high-temperature *Cmcm* phase of SnSe: soft modes and three-phonon interactions

Jonathan M. Skelton, Lee A. Burton, Stephen C. Parker and Aron Walsh*
Department of Chemistry, University of Bath, Claverton Down, Bath, BA2 7AY, UK

Chang-Eun Kim and Aloysius Soon
Department of Materials Science and Engineering, Yonsei University, Seoul, Korea

John Buckeridge, Alexey A. Sokol and C. Richard A. Catlow
University College London, Kathleen Lonsdale Materials Chemistry, Department of Chemistry, 20 Gordon Street, London WC1H 0AJ, United Kingdom

Atsushi Togo and Isao Tanaka
Elements Strategy Initiative for Structural Materials, Kyoto University, Kyoto Prefecture 606-8501, Japan

The layered semiconductor SnSe is one of the highest-performing thermoelectric materials known. We demonstrate, through a first-principles lattice-dynamics study, that the high-temperature *Cmcm* phase is a dynamic average over lower-symmetry minima separated by very small energetic barriers. Compared to the low-temperature *Pnma* phase, the *Cmcm* phase displays a phonon softening and enhanced three-phonon scattering, leading to an anharmonic damping of the low-frequency modes and hence the thermal transport. We develop a renormalisation scheme to quantify the effect of the soft modes on the calculated properties, and confirm that the anharmonicity is an inherent feature of the *Cmcm* phase. These results suggest a design concept for thermal insulators and thermoelectric materials, based on dispersive instabilities, and highlight the power of lattice-dynamics calculations for material characterization.

DOI: XX.YYY/Journal.Vol.PaperRef

PACS Numbers: 05.70.-a, 31.15.A-, 72.20.Pa

Thermoelectrics are an important class of functional materials which interconvert heat and electricity,[1] and are a key component in the drive for “green” energy.[2] The figure of merit for thermoelectric performance is $ZT = S^2\sigma/(\kappa_L + \kappa_{el})$, where S and σ are the Seebeck coefficient and electrical conductivity, and κ_L and κ_{el} are the lattice and electronic thermal conductivities, respectively. The key to developing high-performance thermoelectric materials is to reduce the thermal conductivity while maintaining a high thermopower $S^2\sigma$. Widespread application requires a ZT above 2 at the target operating temperature.[3]

Historically, the lead chalcogenides set the benchmark for high thermoelectric performance due to their unique combination of favourable electrical properties and strongly-anharmonic lattice dynamics.[4-11] However, bulk SnSe was recently shown to be a very promising high-temperature thermoelectric, with a ZT score surpassing the record set by nanostructured PbTe.[12] This has been ascribed to an ultra-low lattice thermal conductivity, arising from its pseudo-layered structure and strong high-temperature anharmonicity.[13,14] Compared to PbTe, SnSe achieves superior thermoelectric performance without the need for doping or other material modifications,[15] which can be detrimental to electrical properties. It is therefore important to elucidate the microscopic origin of its high performance, in order that the same ideas may be incorporated into design strategies for improving thermoelectrics.

SnSe displays a second-order phase change from *Pnma* to *Cmcm* space groups between 700-800 K. Although preliminary studies on SnSe have been carried out,[16] these have not extended to the dynamics of the high-temperature phase and the influence of the phase transition on the thermal transport. Since thermoelectric materials are generally

required to operate at high temperature, understanding this factor is essential to facilitate the tailored design of future functional materials.

Previous theoretical studies have shown that first-principles lattice-dynamics calculations can provide deep insight into the material physics underlying thermoelectric performance.[17-24] In this work, we have employed first-principles lattice-dynamics calculations to model both phases of SnSe, with a particular focus on characterising the lattice dynamics and thermal transport in the high-temperature phase.

Our lattice-dynamics calculations were performed with the Phonopy[25] and Phono3py[26] packages, using the VASP code[27] as the force calculator. We used the PBEsol functional,[28] which we have previously found to give a very good description of the lattice dynamics in a range of semiconductors,[29] in conjunction with projector augmented-wave pseudopotentials and carefully-converged plane-wave cutoff and k -point sampling. The finite-displacement phonon calculations were likewise carried out using carefully-chosen supercell sizes. Full technical details of our simulations are given in the supporting information.[†]

The optimised equilibrium structures of the two phases are shown in Figs. 1c and 1d. The calculated lattice parameters of the *Pnma* and *Cmcm* phases are $a = 4.367$, $b = 11.435$ and $c = 4.151$ Å, and $a = 4.216$ Å, $b = 11.521$ and $c = 4.203$ Å, respectively. These values are consistent with experimental characterization (*Pnma*: $a = 4.44$ Å, $b = 11.49$ Å, $c = 4.135$ Å; *Cmcm*: $a, c = 4.31$ Å, $b = 11.70$ Å), and with other theoretical studies.[13,16] The low-temperature phase is a distortion of the more symmetric high-temperature structure, leading to a primitive unit cell with twice the volume, and both structures can be thought of as distortions to the rocksalt structure of the Pb analogue PbSe.

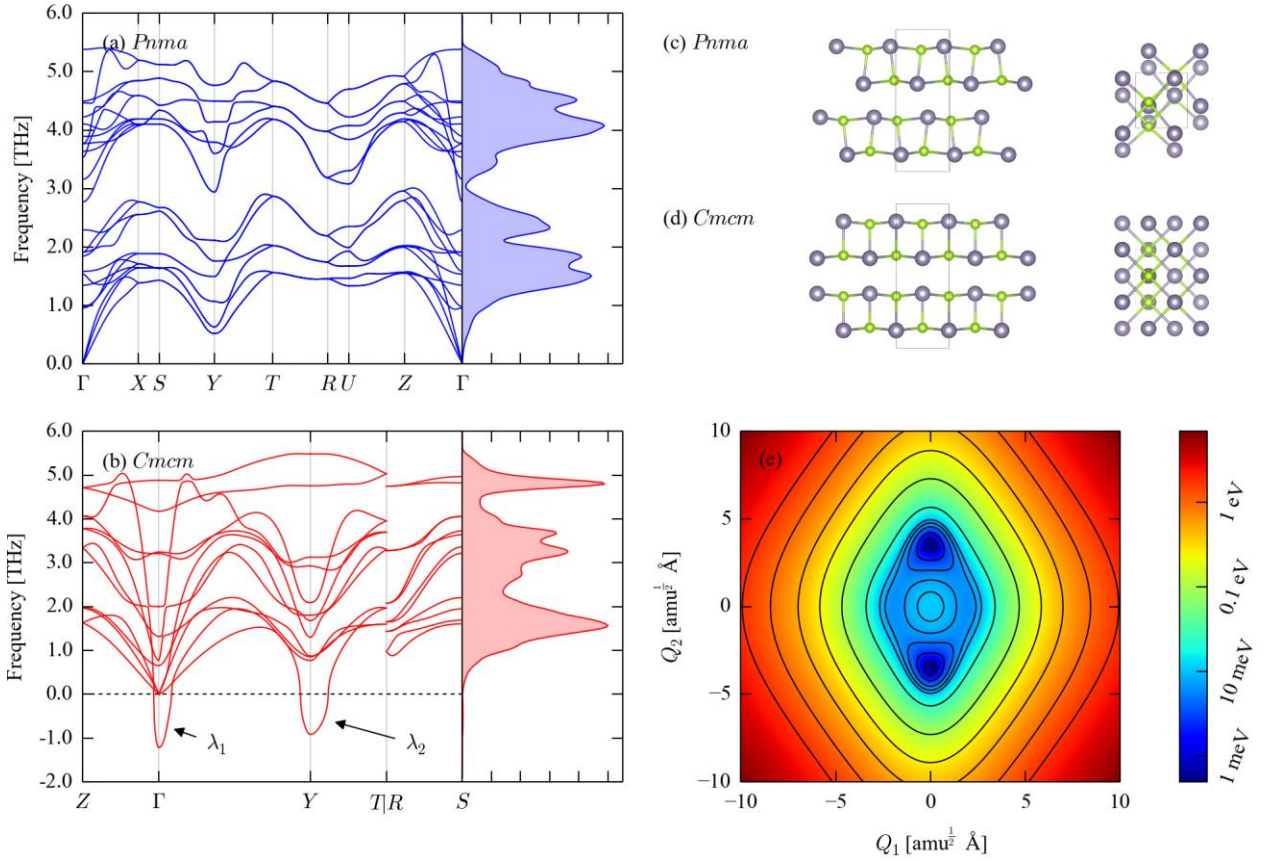


FIG. 1 (Color Online) Lattice dynamics of SnSe. Plots (a) and (b) show the phonon dispersions and densities of states of the optimised equilibrium *Pnma* and *Cmcm* structures illustrated in (c) and (d), respectively. The dispersion of the high-temperature *Cmcm* phase shows imaginary modes at the symmetry points Γ and Y , marked λ_1 and λ_2 respectively. The potential-energy surface along the two corresponding normal-mode coordinates (Q_1/Q_2) is shown in plot (e). The left- and right-hand snapshots in c/d are taken through the *ab* and *ac* planes, respectively, and the Sn and Se atoms in (c) and (d) are coloured green and silver. The images were prepared using VESTA (Ref. [30]).

Comparing the phonon dispersion and density-of-states (DoS) curves of the two phases (Figs. 1a/1b), the upper part of the *Cmcm* DoS displays a noticeable red shift with respect to the *Pnma* phase. From a numerical integration,[†] around 15 % of the states in the low-temperature phase lie between 3-4 THz, compared to ~30 % in the high-temperature phase. Furthermore, whereas the dispersion of the *Pnma* structure shows real (positive) frequencies across the Brillouin zone (Fig. 1a), the dispersion of the high-temperature phase displays prominent imaginary (“negative”) modes at Γ and Y (Fig. 1b). The imaginary modes make an almost negligible contribution to the overall phonon DoS, suggesting them to be localised at the symmetry points, as was the case among the 48 commensurate \mathbf{q} -points in the $8 \times 1 \times 6$ (conventional) supercell used in the present calculations.

The mode at Y in the primitive *Cmcm* cell folds to the zone centre in the conventional cell, allowing the two-dimensional potential-energy surface spanned by the mode eigenvectors to be straightforwardly mapped out (Fig. 1e). From an analysis of the mode eigenvectors,[†] both modes correspond to symmetry-breaking displacive instabilities. Each mode forms an anharmonic double-well potential (Figs. 2a/2c), with the potential along the more negative mode at Γ (λ_1 in Fig. 1 (b)) being steeper, but that along the Y -point mode (λ_2) possessing a deeper minimum. The two pairs of minima are 5 and 11 meV below the average structure, respectively. This indicates that the *Cmcm* phase is effectively an average structure, in a manner analogous to the

high-temperature phases of some oxides[31] and oxide/halide perovskites (e.g. CsSnI_3).[24,32,33] To confirm this, we computed phonon dispersions and DoS curves over a range of expansions and contractions about the athermal equilibrium volume,[†] which indicated that the imaginary modes soften further under lattice expansion, rather than becoming real, and persist under moderate applied pressure.

Soft modes present a challenge to lattice-dynamics calculations, since techniques for treating higher-order anharmonicity (e.g. self-consistent phonon theory[34,35]) are often impractically expensive. Whereas in real systems phonon instabilities are localized to regions of infinitesimal volume in reciprocal space (i.e. points, lines or planes), and thus do not contribute to thermodynamic properties such as the free energy,[31] the finite Brillouin-zone sampling and interpolation used in lattice-dynamics calculations “spreads” the imaginary modes over a finite volume. In order to investigate the effect of the imaginary modes in the high-temperature phase on our calculations, we therefore implemented a simple renormalization scheme to calculate approximate effective harmonic frequencies. The potential energy along each mode as a function of the respective normal-mode coordinate, $Q_{\lambda=1,2}$, is fitted to an eight-power polynomial, and 1D Schrödinger equations for the potentials are solved to obtain the eigenvalues inside the anharmonic double wells (Figs. 2a/2c).

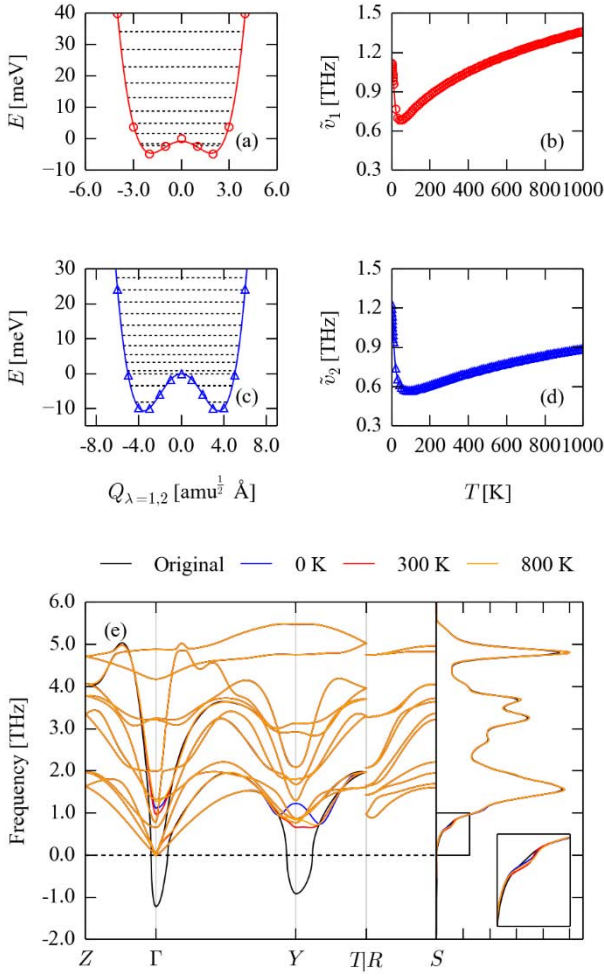


FIG. 2 (Color online) Renormalization of the imaginary harmonic-phonon modes in the equilibrium *Cmcm* SnSe structure. Plots (a) and (c) show the anharmonic double-well potentials along the two modes labelled λ_1 and λ_2 in Fig. 1b as a function of the corresponding normal-mode coordinates $Q_{\lambda=1,2}$. The markers show the calculated points, the solid lines are fits to an eight-power polynomial, and the dotted black lines show the eigenvalues obtained by solving 1D Schrödinger equations for the potentials. Plots (b) and (d) show the effective renormalized frequencies of the two modes ($\tilde{\nu}_{\lambda=1,2}$), calculated as the harmonic frequencies which reproduce the contribution of the mode to the vibrational partition function as a function of temperature. Plot (e) compares phonon dispersions and densities of states calculated without renormalization (black) and with the imaginary modes renormalized to the calculated 0 (blue), 300 (red) and 800 K (orange) frequencies.

Effective (real) harmonic frequencies for the imaginary modes are then calculated as a function of temperature to reproduce the contribution of the modes to the vibrational partition function (Figs. 2b/2d). These effective frequencies are used to adjust the harmonic force constants, by back transforming the dynamical matrices at the commensurate \mathbf{q} -points after adjusting the frequencies at the Γ point (in the conventional cell). These corrected force-constant matrices are then used as input for further post processing. A detailed overview of the renormalization scheme and its implementation is given in the supporting information.[†]

In our model, the renormalized 0 K frequencies of the imaginary modes at Γ and Y are 1.12 and 1.23 THz, respectively. The frequencies initially decrease with temperature, as the system explores higher energy levels

within the minima, and reaches a minimum close to where the available thermal energy is comparable to the barrier height (approx. 40 and 90 K, respectively, for the two modes). Above these temperatures, the renormalized frequencies increase monotonically, as the system accesses the steeper parts of the potential. The renormalized frequencies of the Γ and Y modes at 300 K are 0.971 and 0.659 THz, respectively, and increase to 1.278 and 0.840 THz at 800 K (the temperature above which the *Cmcm* phase is observed crystallographically[13]).

Fig. 2e shows the impact of renormalizing the imaginary modes to the effective 0, 300 and 1000 K frequencies on the phonon dispersion and DoS. The effect on the orthogonal phonon branches is minimal, and the correction is strongly localized towards the symmetry points where the imaginary modes occur. The latter is primarily a result of the large supercell used for calculating the force constants, which we consider a prerequisite for this renormalization scheme. The effect of the renormalization on the phonon DoS is also minimal, with the most notable differences occurring up to ~ 1 THz (Fig. 2e, inset). The renormalization was found to have a negligible impact on thermodynamic functions calculated within the harmonic approximation,[†] with a maximum difference in the high-temperature (1000 K) vibrational Helmholtz free energy being of $< 0.25 \text{ kJ mol}^{-1}$ per SnSe formula unit (c.f. $k_B T = 8.314 \text{ kJ mol}^{-1}$ at this temperature).

To investigate the effect of the phase transition on thermal-transport properties, we calculated third-order force constants for both structures. These were used to obtain phonon lifetimes within the single-mode relaxation-time approximation,[26] and to solve the Boltzmann transport equations to obtain the lattice thermal conductivity as a function of temperature. In these calculations, we did not attempt to correct the third-order force constants for the imaginary modes in the *Cmcm* phase, but instead performed post-processing for the high-temperature structure using second-order force constants corrected with the 800 K renormalized frequencies.

Within the relaxation-time approximation, the phonon lifetimes are calculated from three-phonon interaction strengths, $\phi_{\lambda\lambda'\lambda''}$, obtained from the third-order force constants, plus an expression for the conservation of energy.[26] Neglecting quasi-harmonic effects from volume expansion, $\phi_{\lambda\lambda'\lambda''}$ is temperature independent, and a histogram showing the average phonon-phonon interaction strengths, $P_{\mathbf{q}j}$, across the phonon DoS provides a convenient means to compare the inherent “anharmonicity” of the two phases (Fig. 3 a-c). This comparison clearly shows that the low-frequency modes in the *Cmcm* phase experience a substantially stronger interaction with other phonon modes compared to the lower-frequency branches in the *Pnma* phase. Correcting the second-order force constants reduces the interaction strength up to ~ 0.5 THz, but the average interaction strength up to ~ 3 THz remains consistently higher than in the *Pnma* phase. These calculations therefore indicate that the high-temperature phase is inherently more anharmonic.

The calculated 300 K lattice thermal conductivity (κ_L) of the *Pnma* phase (Fig. 3d) is 1.44, 0.53 and 1.88 $\text{W m}^{-1} \text{K}^{-1}$ along the a , b and c axes, respectively.

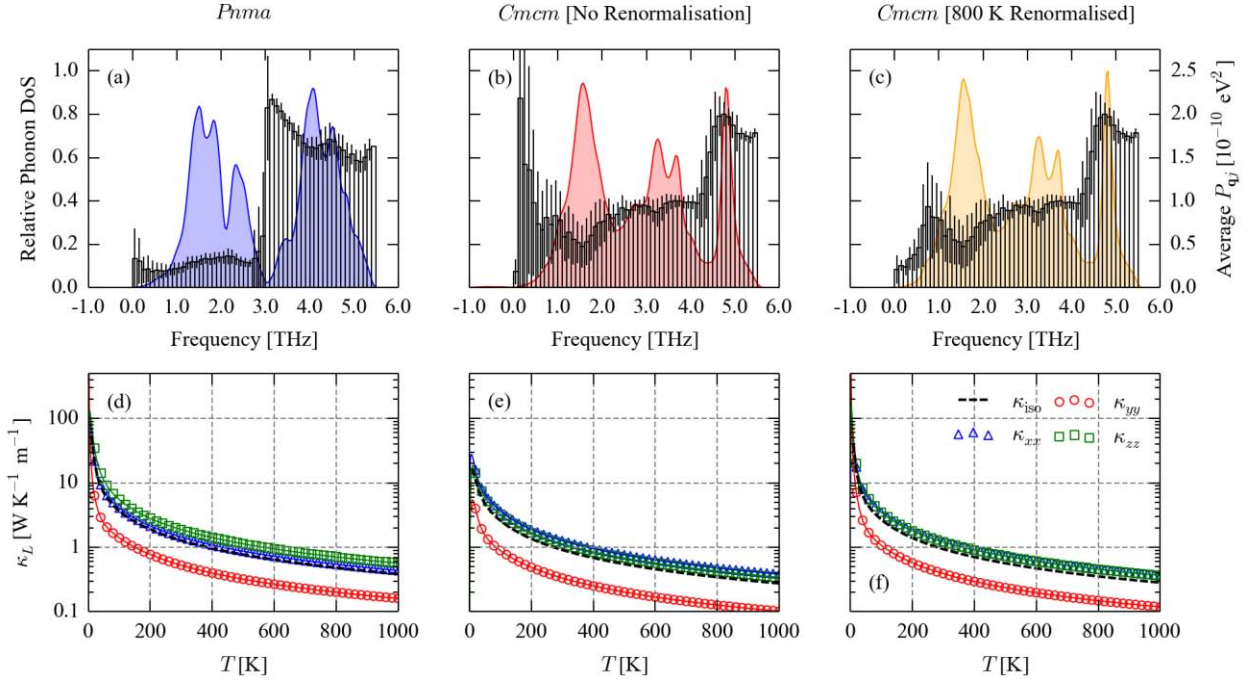


FIG. 3 (Color online) Thermal-transport properties of the *Pnma* (a, d) and *Cmcm* (b, c, e, f) phases of SnSe. Plots (a) - (c) show the averaged three-phonon interaction strengths, $P_{\mathbf{q}j}$ (as defined in Ref. [26]), overlaid on the phonon densities of states. The error bars show the standard deviation on the average in each histogram bin. Plots (d) - (e) show the calculated lattice thermal conductivity (κ_L) along each of the three crystallographic axes, together with the isotropic average. The data *Cmcm*-phase data shown in (b) and (e) was modelled without renormalization of the imaginary modes, while that shown in (c) and (f) was modelled with the second-order (harmonic) force constants corrected using the 800 K renormalized frequencies.

These values are in reasonable agreement with measurements of ~ 0.7 and ~ 0.45 $\text{W m}^{-1} \text{K}^{-1}$ along the two short and one long axes,[13] and the predicted axial anisotropy is consistent with other studies.[13,16] For the *Cmcm* phase (Fig. 3e), we calculated an isotropic average κ_L of 0.34 $\text{W m}^{-1} \text{K}^{-1}$, compared to the measured ~ 0.25 $\text{W m}^{-1} \text{K}^{-1}$. [13] Given the neglect of volume expansion, higher-order anharmonicity and scattering processes in the present calculations, this is again reasonable agreement. As in the *Pnma* phase, these calculations predict an axial anisotropy in κ_L , with significantly reduced transport along the long axis. With the second-order force constants corrected, we calculated an average κ_L of 0.35 (an increase of 3 %), indicating that renormalization has only a small quantitative impact. Analysis of the modal contributions to the thermal transport at 300 and 800 K[†] shows that the low-frequency modes account for the bulk of the heat transport in both phases, and that the larger phonon-phonon interaction strengths in the *Cmcm* phase significantly reduce the lifetimes of these modes, thus explaining its reduced κ_L .

Finally, an important point, not accounted for in the present study, is that the phonon softening in the *Cmcm* phase might be expected to lead to increased thermal expansion, further damping the thermal conductivity.[23] The importance of this latter effect could be probed using our renormalization scheme in conjunction with the quasi-harmonic approximation, a task which, due to the computational cost involved, we leave to a future study.

In summary, our calculations demonstrate that the low high-temperature lattice thermal conductivity SnSe is due to anharmonic damping of the low-frequency phonon modes. We have developed a simple renormalization scheme to

quantify the impact of the phonon instabilities in the high-temperature phase on properties calculated using second-order force constants, and hence shown the enhanced anharmonicity to be an inherent property of this system. This scheme may form a practical basis for studying other important classes of system with displacive instabilities, e.g. halide perovskites. From a materials-design perspective, similar anharmonic phonon damping may occur in other systems at the boundary of a phase transition, and so this could serve as a selection criterion for identifying materials with ultra-low thermal conductivity. In these materials, the poor thermal transport is a bulk property, and so the potential negative impact on electrical properties of modifications such as doping and nanostructuring may be avoided. Understanding this phenomenon may thus provide a robust design strategy for developing thermal insulators and high-performance thermoelectric materials.

We gratefully acknowledge useful discussions with Dr J. M. Frost. JMS is supported by an EPSRC programme grant (grant no. EP/K004956/1). LAB is currently supported by the JSPS (grant no. 26.04792). JB acknowledges support from the EPSRC (grant no. EP/K016288/1). Calculations were carried out on the ARCHER supercomputer, accessed through membership of the UKs HPC Materials Chemistry Consortium, which is funded by the EPSRC (grant no. EP/L000202). We also made use of the Bath University HPC cluster, which is maintained by the Bath University Computing Services.

APPENDIX: Data-access statement

In addition to the data in the electronic supporting information,[†] the optimised structures and raw/processed data from the phonon calculations are available online, free of charge, from <https://github.com/WMD-group/Phonons> [data to be made public on acceptance]. This repository also includes the codes used to implement our approximate renormalization scheme.

*a.walsh@bath.ac.uk

†Electronic supporting information available online at [URL to be added on acceptance] or from the authors.

- [1] J. R. Sootsman, D. Y. Chung, and M. G. Kanatzidis, *Angew Chem Int Edit* **48**, 8616 (2009).
- [2] G. J. Snyder and E. S. Toberer, *Nat. Mater.* **7**, 105 (2008).
- [3] J. F. Li, W. S. Liu, L. D. Zhao, and M. Zhou, *Npg Asia Mater* **2**, 152 (2010).
- [4] R. N. Tauber, A. A. Machonis, and I. B. Cadoff, *Journal of Applied Physics* **37**, 4855 (1966).
- [5] Y. Z. Pei, X. Y. Shi, A. LaLonde, H. Wang, L. D. Chen, and G. J. Snyder, *Nature* **473**, 66 (2011).
- [6] Z. M. Gibbs, H. Kim, H. Wang, R. L. White, F. Drymiotis, M. Kaviani, and G. Jeffrey Snyder, *Applied Physics Letters* **103** (2013).
- [7] E. S. Bozin, C. D. Malliakas, P. Souvatzis, T. Proffen, N. A. Spaldin, M. G. Kanatzidis, and S. J. L. Billinge, *Science* **330**, 1660 (2010).
- [8] O. Delaire *et al.*, *Nat. Mater.* **10**, 614 (2011).
- [9] S. Kastbjerg, N. Bindzus, M. Sondergaard, S. Johnsen, N. Lock, M. Christensen, M. Takata, M. A. Spackman, and B. B. Iversen, *Advanced Functional Materials* **23**, 5477 (2013).
- [10] T. Keiber, F. Bridges, and B. C. Sales, *Physical Review Letters* **111**, 095504 (2013).
- [11] K. S. Knight, *Journal of Physics: Condensed Matter* **26**, 385403 (2014).
- [12] K. Biswas, J. Q. He, I. D. Blum, C. I. Wu, T. P. Hogan, D. N. Seidman, V. P. Dravid, and M. G. Kanatzidis, *Nature* **489**, 414 (2012).
- [13] L.-D. Zhao, S.-H. Lo, Y. Zhang, H. Sun, G. Tan, C. Uher, C. Wolverton, V. P. Dravid, and M. G. Kanatzidis, *Nature* **508**, 373 (2014).
- [14] C. W. Li, J. Hong, A. F. May, D. Bansal, S. Chi, T. Hong, G. Ehlers, and O. Delaire, *Nat Phys* **11**, 1063 (2015).
- [15] J. P. Heremans, *Nature* **508**, 327 (2014).
- [16] J. Carrete, N. Mingo, and S. Curtarolo, *Applied Physics Letters* **105**, 101907 (2014).
- [17] J. M. An, A. Subedi, and D. J. Singh, *Solid State Commun* **148**, 417 (2008).
- [18] A. H. Romero, M. Cardona, R. K. Kremer, R. Lauck, G. Siegle, J. Serrano, and X. C. Gonze, *Physical Review B* **78** (2008).
- [19] Y. Zhang, X. Z. Ke, C. F. Chen, J. Yang, and P. R. C. Kent, *Physical Review B* **80** (2009).
- [20] O. Kilian, G. Allan, and L. Wirtz, *Physical Review B* **80**, 245208 (2009).
- [21] T. Shiga, J. Shiomi, J. Ma, O. Delaire, T. Radzynski, A. Lusakowski, K. Esfarjani, and G. Chen, *Physical Review B* **85** (2012).
- [22] Z. T. Tian, J. Garg, K. Esfarjani, T. Shiga, J. Shiomi, and G. Chen, *Physical Review B* **85** (2012).
- [23] J. M. Skelton, S. C. Parker, A. Togo, I. Tanaka, and A. Walsh, *Physical Review B* **89**, 205203 (2014).
- [24] J. Buckeridge, D. O. Scanlon, A. Walsh, C. R. A. Catlow, and A. A. Sokol, *Physical Review B* **87** (2013).
- [25] A. Togo, F. Oba, and I. Tanaka, *Physical Review B* **78**, 134106 (2008).
- [26] A. Togo, L. Chaput, and I. Tanaka, *Physical Review B* **91**, 094306 (2015).
- [27] G. Kresse and J. Hafner, *Physical Review B* **47** (1993).
- [28] J. P. Perdew, A. Ruzsinszky, G. I. Csonka, O. A. Vydrov, G. E. Scuseria, L. A. Constantin, X. L. Zhou, and K. Burke, *Physical Review Letters* **100** (2008).
- [29] J. M. Skelton, D. Tiana, S. C. Parker, A. Togo, I. Tanaka, and A. Walsh, *J. Chem. Phys.* **143** (2015).
- [30] K. Momma and F. Izumi, *J Appl Crystallogr* **44**, 1272 (2011).
- [31] M. T. Dove, *Am Mineral* **82**, 213 (1997).
- [32] L.-y. Huang and W. R. L. Lambrecht, *Physical Review B* **90**, 195201 (2014).
- [33] E. L. da Silva, J. M. Skelton, S. C. Parker, and A. Walsh, *Physical Review B* **91**, 144107 (2015).
- [34] Werthame.Nr, *Phys Rev B-Solid St* **1**, 572 (1970).
- [35] I. Errea, M. Calandra, and F. Mauri, *Physical Review B* **89** (2014).

Anharmonicity in the high-temperature *Cmcm* phase of SnSe: soft modes and three-phonon interactions

J. M. Skelton, L. A. Burton, S. C. Parker and A. Walsh

Department of Chemistry, University of Bath, Claverton Down, Bath, BA2 7AY, UK

C. E. Kim and A. Soon

Department of Materials Science and Engineering, Yonsei University, Seoul, Korea

J. Buckeridge, A. A. Sokol and C. R. A. Catlow

*University College London, Kathleen Lonsdale Materials Chemistry, Department of Chemistry,
20 Gordon Street, London WC1H 0AJ, United Kingdom*

A. Togo and I. Tanaka

*Elements Strategy Initiative for Structural Materials, Kyoto University,
Kyoto Prefecture 606-8501, Japan*

Electronic supporting information

1. *Ab initio* lattice-dynamics calculation protocol

First-principles calculations were carried out within the pseudopotential plane-wave density-functional theory formalism, as implemented in the Vienna *ab initio* Simulation Package (VASP) code.[1] We used projector augmented-wave (PAW) pseudopotentials,[2,3] treating the Sn 4d electrons as valence states, in conjunction with the PBEsol exchange-correlation functional and a plane-wave basis with a kinetic-energy cutoff of 500 eV.[4] An $8\times 4\times 8$ Monkhorst-pack \mathbf{k} -point mesh[5] was used to sample the first Brillouin zone of the conventional *Pnma* and *Cmcm* cells, which was correspondingly reduced for the supercell-phonon calculations. The PAW projection was performed in reciprocal space, and non-spherical contributions to the gradient corrections inside the PAW spheres were taken into account. The electronic structure calculations are performed within the scalar relativistic approximation, excluding spin-orbit coupling.

During geometry optimizations, a tolerance of 10^{-8} eV was applied to the electronic wavefunctions, and the ion positions and lattice parameters were optimized until the magnitude of the forces on the ions was $< 10^{-2}$ eV \AA^{-1} .

Lattice-dynamics calculations were performed with the Phonopy[6] and Phono3py[7] packages, which were used to obtain sets of second- and third-order force-constant matrices, respectively, *via* the supercell finite-displacement method.[8] Second-order force constants were calculated on $6\times 1\times 6$ and $8\times 1\times 6$ expansions of the conventional *Pnma* and *Cmcm* cells, containing 288 and 384 atoms, respectively, with a step size of 10^{-2} \AA . We found that these cells were sufficiently large to converge the shape of the phonon density of states (DoS), with the larger *Cmcm* expansion being required to remove an interpolation artefact along one of the branches of the phonon dispersion (see Section 2, below). Due to the unfavourable scaling of the number of inequivalent two-atom displacements with supercell size, the third-order force constants for both phases were calculated from $3\times 1\times 3$ supercell expansions containing 72 atoms, using a step size of 0.03 \AA . During the post processing, the phonon DoS and lifetimes were sampled on $48\times 48\times 48$ and $16\times 16\times 16$ Γ -centred \mathbf{q} -point grids, respectively.

2. Supercell-size convergence for the finite-displacement calculations

As noted in Section 1 above, it was necessary carefully to converge the supercell size used in the finite-displacement calculations on the *Cmcm* phase of SnSe, in order both to converge the shape of the phonon DoS, and to remove an apparent interpolation artefact along the segment Γ - Y in the phonon dispersion. Table S1 lists the supercell sizes considered during these convergence tests, together with the number of atoms and commensurate \mathbf{q} -points in each (i.e. the number of \mathbf{q} -points at which the phonon frequencies and eigenvectors can be calculated exactly for the given expansion).

In our optimised *Cmcm* structure, the a and c axes are similar in length, and both are significantly shorter than the b axis ($a = 4.216$, $b = 11.521$ and $c = 4.203$ \AA , in the equilibrium structure used in these tests). We therefore first considered expansions of 2, 4, 6 and $8\times$ along the a and c axes, together with expansions of 1 and $2\times$ along the b axis. The calculated phonon band structures and DoS curves are shown in Fig. S1; we note that an $8\times 2\times 8$ expansion would require calculations on 1,024-atom supercells, and we found when attempting these that they required an impractical amount of computing resources with the tight convergence criteria needed to obtain accurate forces.

When a relatively small $2\times$ expansion along the a and c axes is employed, a third imaginary mode, in addition to those at Γ and Y , appears along the segment Γ - Y . This appears to harden when 4 and $6\times$ expansions along the short direction are used, and becomes real for an $8\times$ expansion. Going from a $2\times$ to a $4\times$ expansion along the short axes, there are noticeable changes to the shape of the DoS, particularly in the region between approx. 2 - 4 THz, while further, more subtle changes, mostly in a peak centred around 3.5 THz, occur when the expansion is increased to 6 and $8\times$. Performing

a $2\times$ expansion along the b axis makes has comparatively little effect, and the shape of the DoS computed with the $6\times 1\times 6$ and $6\times 2\times 6$ supercells is very similar.

Supercell	# Atoms	# \mathbf{q} -Points
$1\times 1\times 1$	8	1 (2)
$2\times 1\times 2$	32	4 (8)
$2\times 2\times 2$	64	8 (16)
$4\times 1\times 2$	64	8 (16)
$4\times 1\times 4$	128	16 (32)
$4\times 2\times 4$	256	32 (64)
$6\times 1\times 6$	288	36 (72)
$6\times 2\times 6$	576	72 (144)
$8\times 1\times 2$	128	16 (32)
$8\times 1\times 4$	256	32 (64)
$8\times 1\times 6$	384	48 (96)
$8\times 1\times 8$	512	64 (128)
$8\times 2\times 2$	256	32 (64)
$8\times 2\times 4$	512	64 (128)

Table S1 List of expansions tested during the supercell-size convergence tests on the *Cmcm* structure, together with the number of atoms and commensurate \mathbf{q} -points in each. As a result of the C -centering, the conventional cell has twice the volume of the primitive cell, and a supercell expansion with a given number of commensurate points in the conventional Brillouin zone includes twice as many points in the primitive Brillouin zone, which is indicated by the numbers in brackets in the third column.

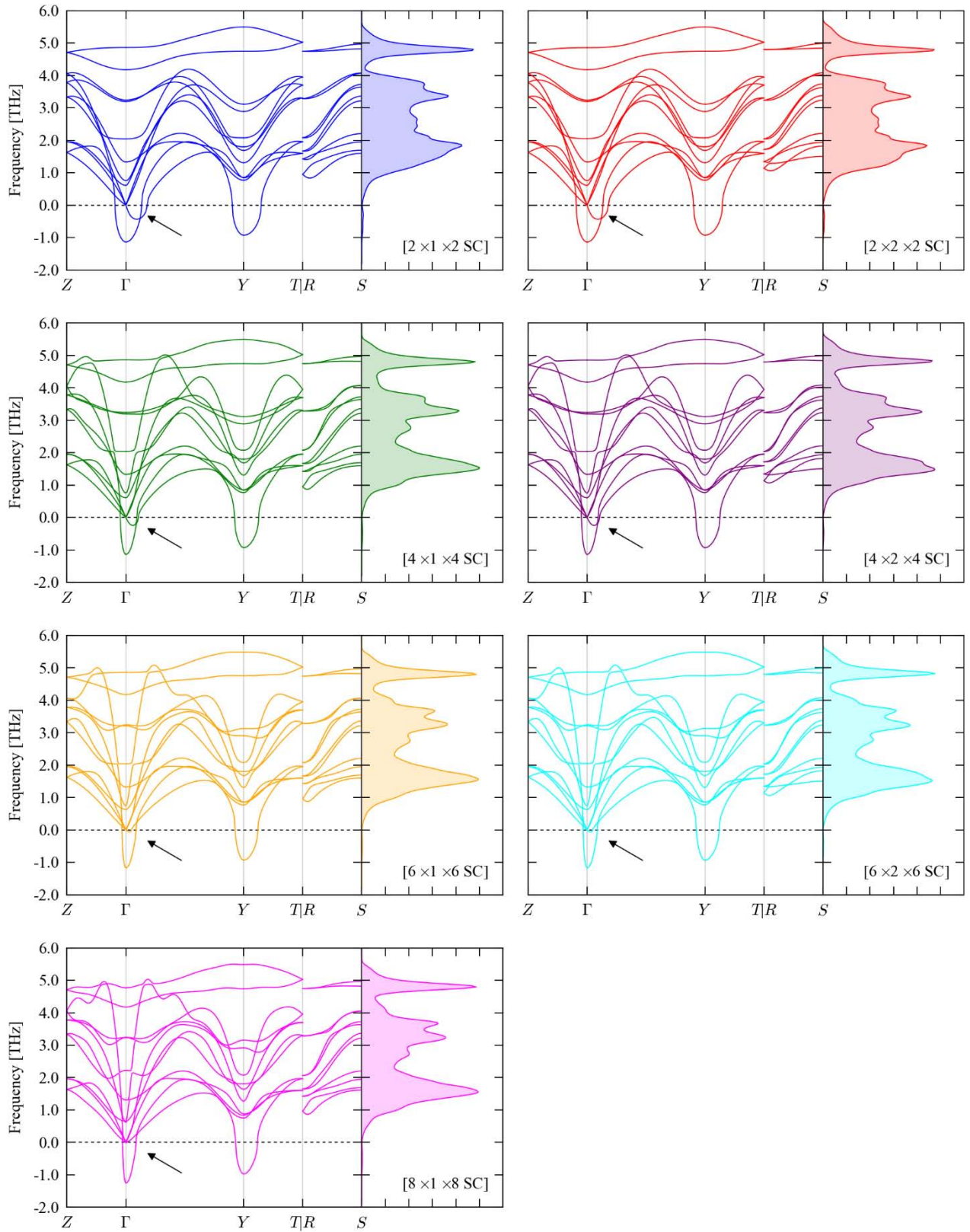


Figure S1 Phonon dispersions and density-of-states curves for the equilibrium structure of *Cmcmm* SnSe, computed using expansions of 2, 4, 6 and 8× along the *a* and *c* axes, together with 1 and 2× expansions along the *b* axis, to evaluate the force-constant matrices.

The $8 \times 1 \times 8$ supercell expansion contains 512 atoms, making the phonon calculations unwieldy. The segment along which the artefact in the phonon dispersions is observed corresponds in real space to the a direction, and so we opted to perform additional tests on supercells with an $8 \times$ expansion along the a direction in conjunction with various expansions along the b and c directions (Fig. S2). From this comparison, an $8 \times 1 \times 6$ expansion, with a more manageable 384 atoms, appears to remove the artefact in the band dispersion while giving a well converged DOS with respect to the larger supercell calculations.

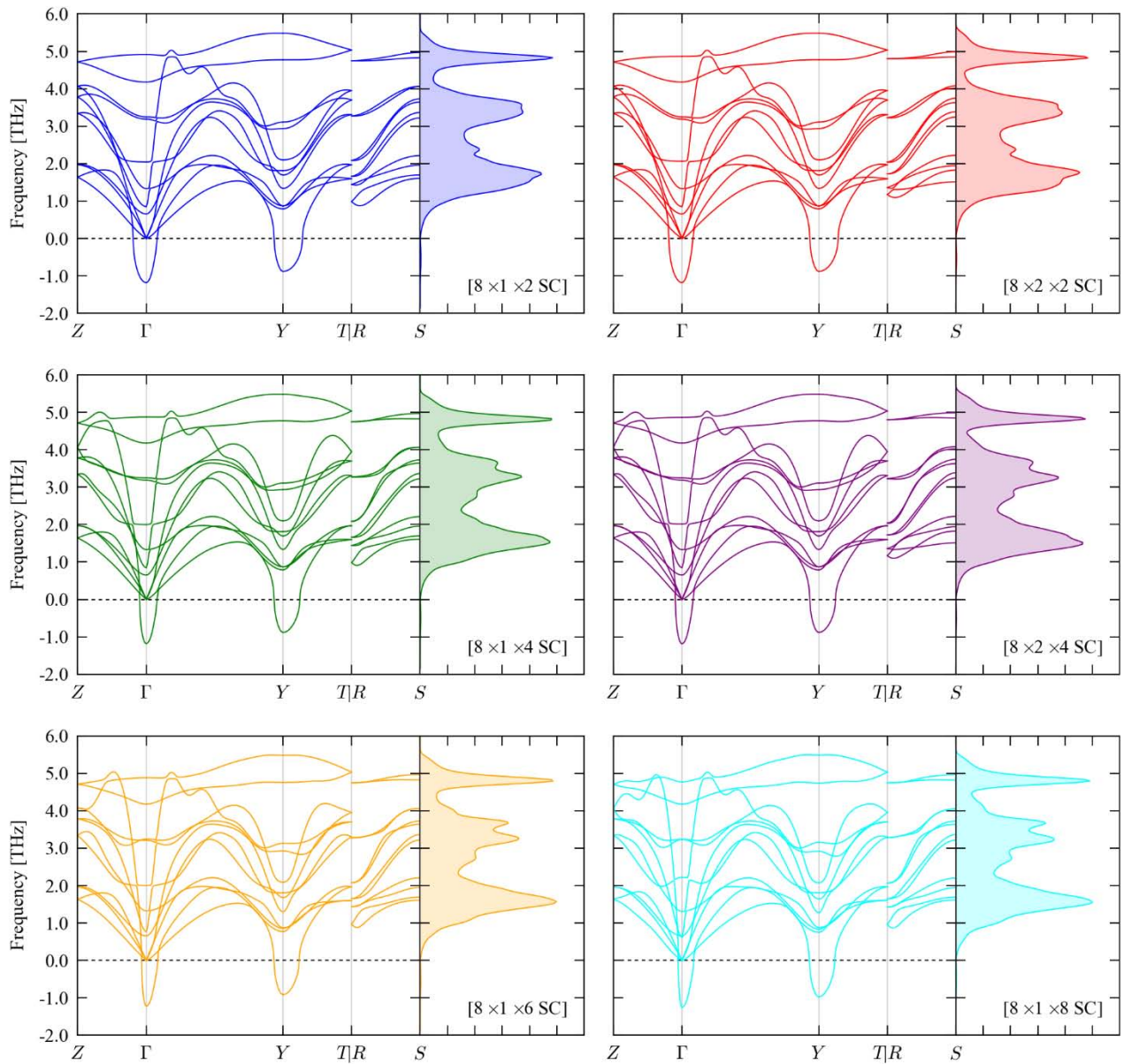


Figure S2 Phonon dispersions and density-of-states curves for the equilibrium structure of *Cmcmm* SnSe, computed using an $8 \times$ expansion along the a axis, paired with expansions of 2, 4, 6 and $8 \times$ along the c axis and 1 and $2 \times$ expansions along the b axis, to obtain the force-constant matrices.

A more quantitative way to assess the supercell-size convergence is the vibrational constant-volume (Helmholtz) free energy, A_{vib} , which is computed by summation over a grid of \mathbf{q} -points sampling reciprocal space according to (eq. S1):

$$A_{vib} = -k_B T \ln \left[\prod_{\lambda} \frac{\exp(-\hbar\omega_{\lambda}/2k_B T)}{1 - \exp(-\hbar\omega_{\lambda}/k_B T)} \right] \quad (\text{S1})$$

k_B is the Boltzmann constant, T is the temperature, and the product runs over phonon modes λ with frequencies ω_{λ} .

We therefore also compared high-temperature (1000 K) free energies computed from calculations performed with the different supercell sizes (Table S2). Taking the $2 \times 1 \times 2$ supercell, which is a reasonable absolute minimum for this system, as a reference, the largest deviation was found to be $0.775 \text{ kJ mol}^{-1}$ per SnSe formula unit (i.e. $< 1 \%$). This is an order of magnitude smaller than $k_B T$ at this temperature ($8.314 \text{ kJ mol}^{-1}$), and is at least comparable to the error one would expect from using an approximate exchange-correlation functional, which suggests that the free energies are relatively insensitive to the set of force-constant matrices.

Supercell	# \mathbf{q} -Points	$A_{vib,1000\text{K}}$ [kJ mol ⁻¹ Per F.U.]	Δ [kJ mol ⁻¹ Per F.U.]
$1 \times 1 \times 1$	1	-114.428	-
$2 \times 1 \times 2$	4	-104.800	0.000
$2 \times 2 \times 2$	8	-104.614	0.186
$4 \times 1 \times 2$	8	-104.357	0.443
$4 \times 1 \times 4$	16	-105.072	-0.272
$4 \times 2 \times 4$	32	-104.924	-0.124
$6 \times 1 \times 6$	36	-105.073	-0.273
$6 \times 2 \times 6$	72	-104.930	-0.130
$8 \times 1 \times 2$	16	-104.203	0.597
$8 \times 1 \times 4$	32	-104.899	-0.099
$8 \times 1 \times 6$	48	-105.075	-0.275
$8 \times 1 \times 8$	64	-105.145	-0.345
$8 \times 2 \times 2$	32	-104.025	0.775
$8 \times 2 \times 4$	64	-104.746	0.054

Table S2 High-temperature (1000 K) constant-volume (Helmholtz) vibrational free energies, $A_{vib,1000\text{K}}$, of equilibrium *Cmcm* SnSe, computed from harmonic-phonon calculations performed with the different supercell sizes in Table S1.

Based on these considerations, we opted to perform our “production” calculations on the *Cmcm* phase using $8 \times 1 \times 6$ supercell expansions of the conventional cell.

Similar convergence tests were also performed on the equilibrium *Pnma* structure. Tables S3 lists the supercell sizes tested, along with the corresponding numbers of atoms and commensurate \mathbf{q} -points. Fig. S3 compares the phonon dispersions and DoS curves obtained using the different expansions, and Table S4 compares the high-temperature vibrational free energies. As for the *Cmcm* structure, we found that large supercell expansions along the short axes were required to converge the shape of the DoS, whereas expanding along the *b* axis led to rather more subtle changes. We also found, again as for the high-temperature phase, that the free energy was relatively insensitive to the choice of

supercell size, differing by a maximum of 0.672 kJ mol⁻¹ per formula unit, which is again an order of magnitude smaller than $k_B T$. Based on these considerations, we selected a similar 6×1×6 expansion for our calculations on the low-temperature phase, as a balance between a good Brillouin-zone sampling and computational cost.

Supercell	# Atoms	# q -Points
2×1×2	32	4
2×2×2	64	8
4×1×4	128	16
4×2×4	256	32
6×1×6	288	36
6×2×6	576	72
8×1×8	512	64

Table S3 List of expansions tested during the supercell-size convergence tests on the *Pnma* structure, together with the number of atoms and commensurate **q**-points in each.

Supercell	# q -Points	$A_{vib,1000K}$ [kJ mol ⁻¹ Per F.U.]	Δ [kJ mol ⁻¹ Per F.U.]
2×1×2	4	-102.070	0.000
2×2×2	8	-101.721	0.349
4×1×4	16	-101.863	0.208
4×2×4	32	-101.666	0.404
6×1×6	36	-101.796	0.274
6×2×6	72	-101.620	0.450
8×1×8	64	-101.398	0.672

Table S4 High-temperature (1000 K) constant-volume (Helmholtz) vibrational free energies, $A_{vib,1000K}$, of equilibrium *Pnma* SnSe, computed from harmonic-phonon calculations with the different supercell sizes in Table S3.

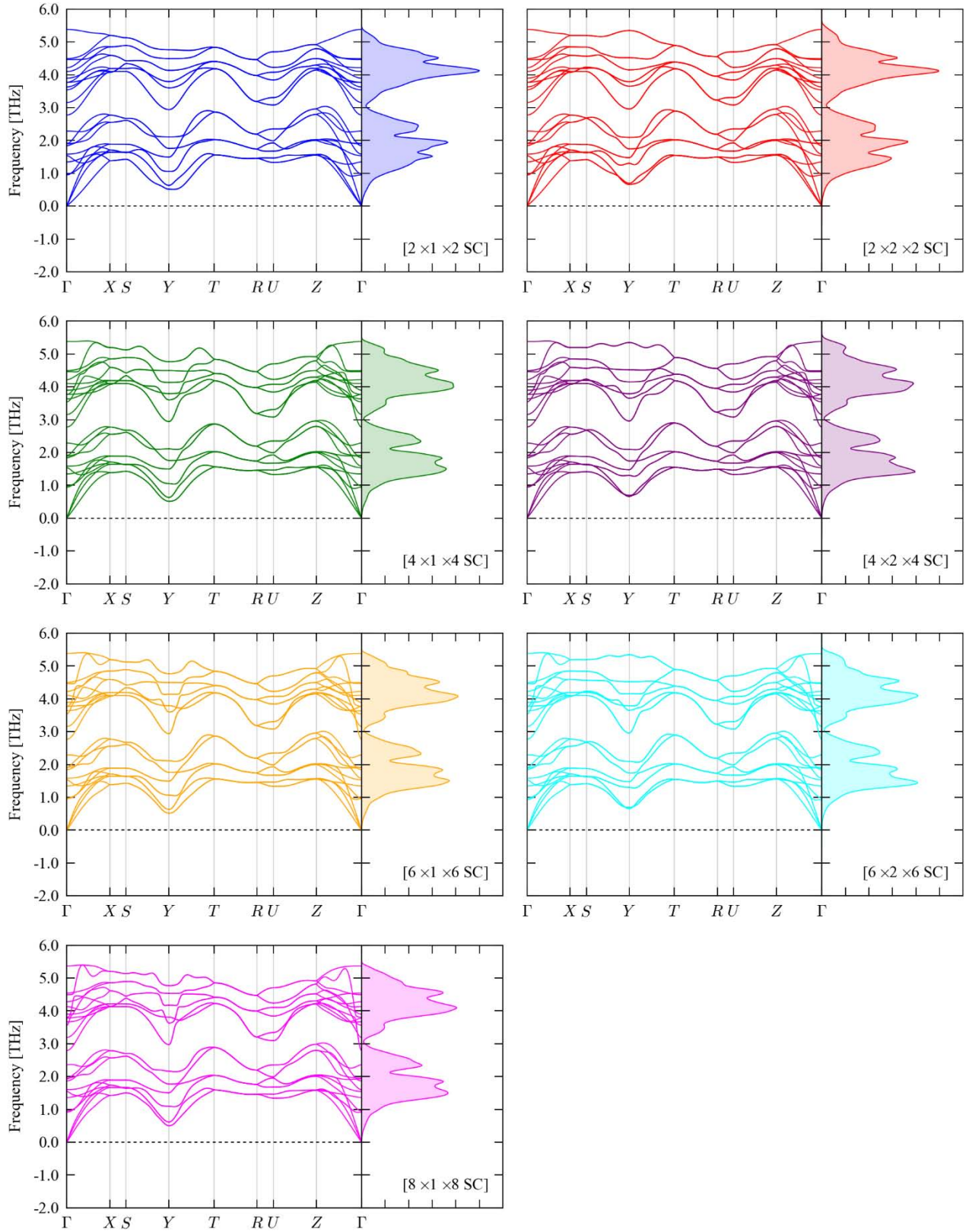


Figure S3 Phonon dispersion and density-of-states curves for the equilibrium structure of *Pnma* SnSe, computed using expansions of 2, 4, 6 and 8× along the *a* and *c* axes, together with 1 and 2× expansions along the *b* axis, to evaluate the force-constant matrices.

3. Numerical integral of the phonon densities of states

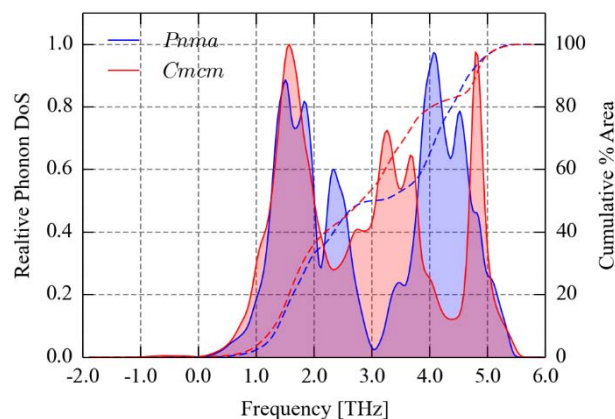


Figure S4 Comparison of the phonon density-of-states (DoS) curves for the equilibrium *Pnma* (blue) and *Cmc* (red) SnSe structures, showing a red shift of the higher-frequency modes (with frequencies > 3 THz) in the latter compared to the former. The two dashed lines show the cumulative percentage of states under each curve as a function of frequency, allowing the shift to be quantified. As stated in the text, whereas there are a similar number of states below 3 THz in both phases, between 3-4 THz there are ~15 % more states in the *Cmc* phase than in the *Pnma* one.

4. Eigenvectors of the imaginary modes in the equilibrium *Cmcm* structure

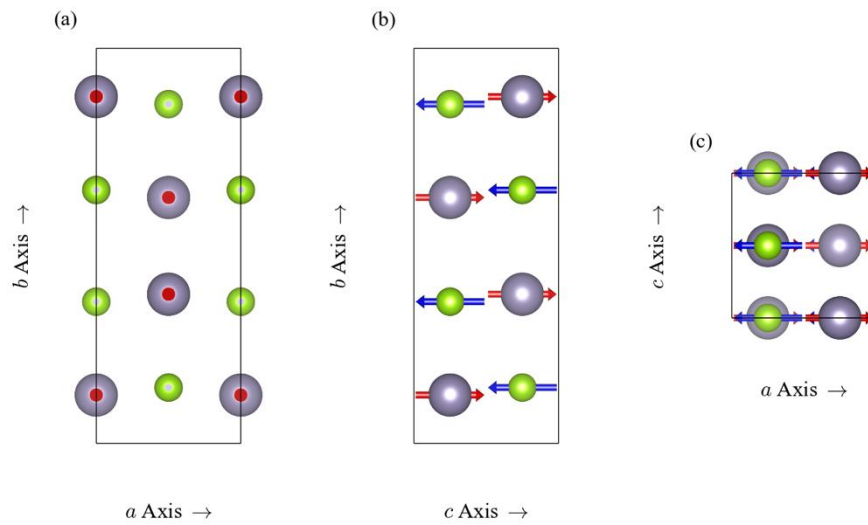


Figure S5 Eigenvectors of the imaginary mode with $\nu = -1.220$ THz in the conventional cell of the equilibrium *Cmcm* SnSe structure. This corresponds to the imaginary mode at Γ in the primitive cell (labelled λ_1 in Figure 1b in the text). The eigenvectors are shown in the *ab* (a), *bc* (b) and *ac* (c) planes. The arrows indicate the direction, but not the magnitude, of the atomic displacements. The images were prepared with the VESTA software.[9]

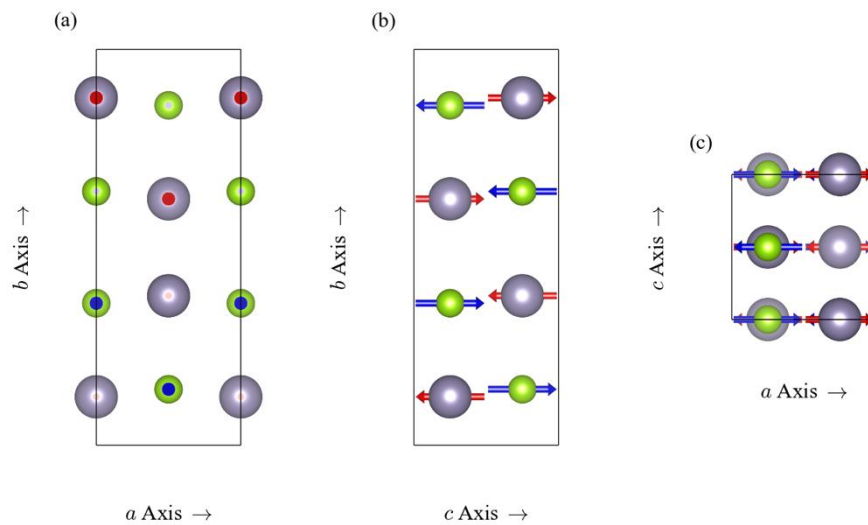


Figure S6 Eigenvectors of the imaginary mode with $\nu = -0.915$ THz in the conventional cell of the equilibrium *Cmcm* SnSe structure. This corresponds to the imaginary mode at Y in the primitive cell (labelled λ_2 in Figure 1b in the text). The eigenvectors are shown in the *ab* (a), *bc* (b) and *ac* (c) planes. The arrows indicate the direction, but not the magnitude, of the atomic displacements. The images were prepared with the VESTA software.[9]

5. Volume dependence of the *Cmcm* phonon dispersion and density of states

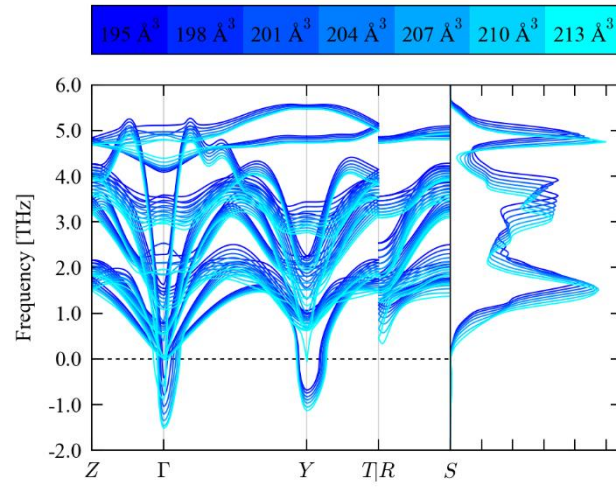


Figure S7 Volume dependence of the phonon dispersion and density of states of *Cmcm* SnSe. The lines are color coded from blue to cyan, corresponding to compressions and expansions, respectively, about the equilibrium volume. The smallest volume corresponds to a hydrostatic pressure of 2.17 GPa. As noted in the text, the imaginary modes at the Γ and Y symmetry points soften under expansion and harden under compression, but persist over the range of volumes examined.

6. Imaginary-mode mapping and renormalization scheme

The potential-energy surfaces along the two imaginary modes in the equilibrium *Cmcm* structure (Figs. 1e and 2a/c in the text) were mapped by performing single-point total-energy calculations on a series of structures of the conventional cell with atomic displacements along the mode eigenvectors over a range of amplitudes “frozen in”. Given the mode eigenvectors \mathbf{W}_λ of a set of phonon modes λ , together with the corresponding normal-mode coordinates (amplitudes) Q_λ , the displacement $\mathbf{u}_{j,l}$ of the j th atom in the l th unit cell can be calculated according to:

$$\mathbf{u}_{j,l} = \frac{1}{\sqrt{Nm_j}} \sum_{\lambda} Q_{\lambda} \exp[-i\mathbf{q}_{\lambda} \cdot \mathbf{r}_{jl}] \mathbf{W}_{\lambda,j} \quad (\text{S2})$$

where $\mathbf{W}_{\lambda,j}$ is the component of \mathbf{W}_λ on atom j , m_j are the atomic masses, N is the number of unit cells, \mathbf{q}_{λ} is the phonon wavevector and \mathbf{r}_{jl} the position of the atom. We note that Q_{λ} absorbs the time dependence of the position.

As noted in the text, the mode at Y in the Brillouin zone of the *Cmcm* primitive cell folds to Γ in the reciprocal space of the conventional cell. In the special case of mapping Γ -point modes in a single unit cell, Eq. S2 can be simplified to:

$$\mathbf{u}_{j,l} = \frac{1}{\sqrt{m_j}} \sum_{\lambda} Q_{\lambda} \mathbf{W}_{\lambda,j} \quad (\text{S3})$$

In the present study, the potential-energy surface was mapped for values of $Q_i = \pm 10 \text{ amu}^{\frac{1}{2}} \text{ \AA}$ in 21 steps including the equilibrium structure. The resulting E/Q_i curves were fitted to eight-power polynomial functions, which were used as input to a program written to solve a 1D Schrödinger equation (1D SE) for the potential to obtain the energy levels (eigenvalues) within the double wells (Figs. 2a/2c in the text).

Each polynomial was evaluated initially on a 1D grid of 256 Q points, and the resulting potential substituted into the 1D SE and solved for the eigenvalues and eigenvectors by means of a Fourier transform followed by matrix diagonalization using the EISPACK routines.[10] This procedure and its advantages compared to solutions in real space are explained in detail in Ref. [11], and we have verified its efficiency against more conventional “shooting method” approaches. The extent of the potential in Q and the grid density are both varied until its effect on the relevant calculated eigenvalues is negligible (i.e. a change of less than 10^{-9} eV).

The eigenvalues, E_i , are used to determine the partition function, Z , via:

$$Z(T) = \sum_i e^{-E_i/k_B T} \quad (\text{S4})$$

where k_B is the Boltzmann constant and T is the temperature. The number of terms included is chosen so that the addition of the final term changes Z by less than 10^{-6} . By setting this expression for Z equal to the harmonic partition function:

$$Z_{\text{harm}}(T) = \sum_n e^{-\left(n+\frac{1}{2}\right)\hbar\tilde{\omega}(T)/k_B T} \quad (\text{S5})$$

where $\tilde{\omega}$ is the effective harmonic frequency, we can derive that (overleaf):

$$\tilde{\omega}(T) = \frac{2k_B T}{\hbar} \sinh^{-1} \left(\frac{1}{2Z(T)} \right) \quad (\text{S6})$$

which provides an effective renormalized harmonic frequency for the mode at a target temperature T .

Finally, these effective frequencies were used to adjust the force constants using the Python API exposed by the Phonopy code.[6] The original force/displacement sets and corresponding force constants were used to calculate the phonon frequencies and eigenvectors in the conventional cell at the \mathbf{q} -points commensurate with our chosen supercell expansions. The frequencies of the imaginary modes at the Γ point were then set to the calculated effective (real) ones, and the corrected dynamical matrices back-transformed to a new set of force constants to be used in subsequent post-processing steps. A short script for patching the force constants, using the Phonopy API, is available as additional data (see Appendix in the main text).

7. Effect of renormalisation on thermodynamic functions

To quantify the effect of renormalizing the imaginary modes in the equilibrium *Cmcm* structure on the thermodynamic functions derived within the harmonic approximation, we compared the temperature dependence of four quantities, viz. the constant-volume vibrational (Helmholtz) free energy, A_{vib} , the constant-volume heat capacity, C_V , the vibrational internal energy, U_{vib} , and the vibrational entropy, S_{vib} , computed with and without renormalizing the imaginary modes. We compared the original curves, i.e. computed without renormalization, to those computed with the imaginary modes renormalized to three constant values, viz. the effective 0, 300 and 1000 K frequencies calculated within our renormalization scheme, and to the renormalized frequency at each temperature-sampling point (see Figs. 2b/2d in the text). The results are shown in Fig. S8, and the calculated vibrational zero-point energies (U_{ZP}) and 1000 K free energies ($A_{vib,1000K}$) are collected in Table S5.

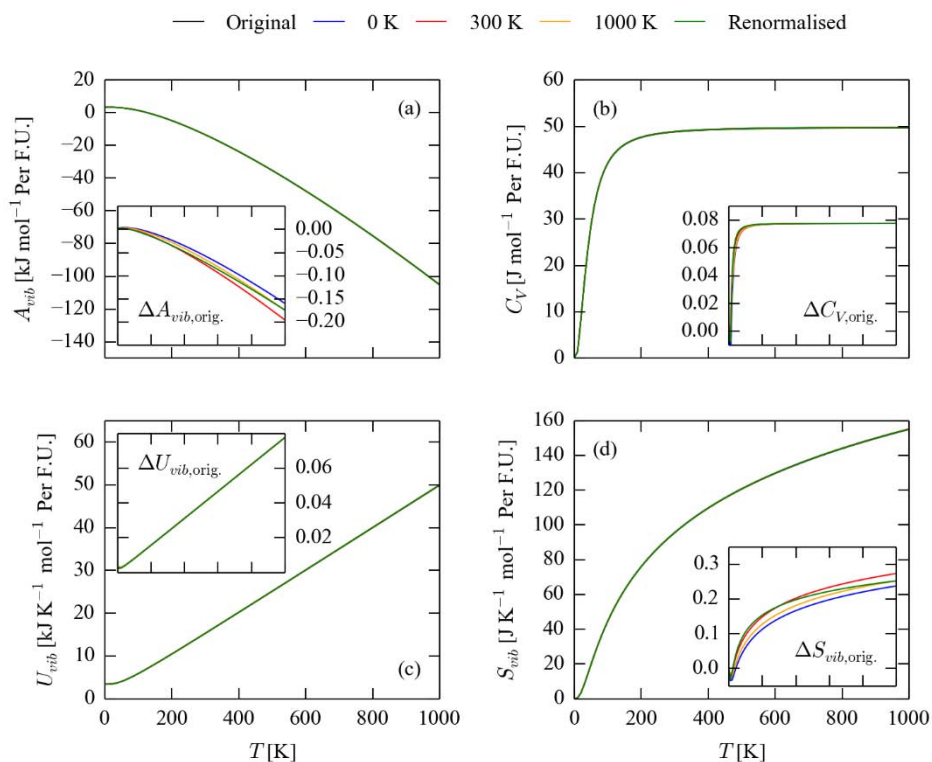


Figure S8 Effect of imaginary-mode renormalization on the temperature-dependent constant-volume vibrational (Helmholtz) free energy (A_{vib} ; a), constant-volume heat capacity (C_V ; b), vibrational internal energy (U_{vib} ; c) and vibrational entropy (S_{vib} ; d). Each plot compares the thermodynamic functions computed using the original phonon frequencies (i.e. without renormalisation; black) and with the imaginary modes renormalized to the (constant) 0 (blue), 300 (red) and 1000 K (orange) frequencies. The green curves were computed by calculating the thermodynamic functions at each temperature-sampling point, i.e. with the imaginary modes renormalized to the corresponding frequencies in Figs. 2b/2d in the text. The inset plots show the difference of the four sets of functions computed with the various renormalization methods to the functions calculated without renormalization.

The data in Table S5 suggests that the renormalization has a minimal impact on the free energy, leading to differences in the zero-point energy on the order of 10^{-3} kJ mol⁻¹ per SnSe formula unit, and to differences in the high-temperature free energy of < 0.25 kJ mol⁻¹ ($\sim 0.25\%$). This is an order of magnitude smaller than $k_B T$ at 1000 K (8.314

kJ mol⁻¹). From the comparison in Fig. S7, this difference occurs predominantly as a result of an increase in S_{vib} , although there is also a small increase in U_{vib} , which is roughly the same for all four renormalized curves. Of most relevance to the thermal conductivity is a small shift in the rising edge of C_V below ~200 K, although this is again relatively small.

Renormalization	[THz]		[kJ mol ⁻¹ Per SnSe F.U.]	
	$\tilde{\nu}_1$	$\tilde{\nu}_2$	U_{ZP}	$A_{vib,1000K}$
None	-1.220	-0.915	3.393	-105.075
0 K	1.115	1.226	3.392	-105.235
300 K	0.971	0.659	3.392	-105.271
1000 K	1.360	0.890	3.393	-105.249
T dep.	-	-	3.393	-105.249

Table S5 Calculated vibrational zero-point energies (U_{ZP}) and 1000 K constant-volume (Helmholtz) free energies ($A_{vib,1000K}$) without renormalization of the imaginary modes, and with the imaginary modes renormalized to three constant values, *viz.* the calculated 0, 300 and 1000 K frequencies, and to the calculated frequency at each temperature-sampling point (Figs. 2b/2d in the text). For the first four rows, the original/renormalized frequencies of the two imaginary modes marked in Fig. 1b in the text ($\tilde{\nu}_{\lambda=1,2}$) that were used are listed. We note that the U_{ZP} and $A_{vib,1000K}$ values for the temperature-dependent renormalization are the same as those for the 0 and 1000 K constant renormalized frequencies, respectively.

8. Detailed analysis of the thermal transport in the *Pnma* and *Cmcm* phases

To investigate the origin of the reduction in lattice thermal conductivity (κ_L) between the low-temperature *Pnma* and high-temperature *Cmcm* phases, we performed a detailed analysis of the modal contributions to the room-temperature (300 K) and 800 K lattice thermal conductivities of the two phases.

A comparison of the cumulative lattice thermal conductivity as a function of phonon frequency for the *Pnma* phase at 300 K against the phonon DoS (Fig. S9a) indicates that ~ 70 % of the heat transport is due to the lower-frequency modes (with frequencies $< \sim 3$ THz). This rises to around 80 % in the *Cmcm* phase (Fig. S9b), which can be explained by the red shift of some of the high-frequency modes discussed in the text (see also Section 3, above). Renormalizing the soft modes has little effect on the shape of the DoS nor the cumulative thermal conductivity distribution (Fig. S8c). A similar comparison at 800 K (Fig. S13) gives a practically identical analysis.

Within the single-mode relaxation-time approximation, the macroscopic thermal-conductivity tensor is obtained as a summation of modal contributions according to:[7]

$$\kappa_L = \frac{1}{NV_0} \sum_{\lambda} C_{\lambda} \mathbf{v}_{g,\lambda} \otimes \mathbf{v}_{g,\lambda} \tau_{\lambda} \quad (\text{S7})$$

where N is the number of unit cells in the crystal, V_0 is the unit-cell volume, C_{λ} are the modal heat capacities, $\mathbf{v}_{g,\lambda}$ are the mode group velocities, and τ_{λ} are the mode lifetimes. The group velocities and modal heat capacities are calculable within the harmonic approximation according to:

$$C_{\lambda} = k_B \left(\frac{\hbar \omega_{\lambda}}{k_B T} \right)^2 \frac{\exp(\hbar \omega_{\lambda}/k_B T)}{[\exp(\hbar \omega_{\lambda}/k_B T) - 1]^2} \quad (\text{S8})$$

$$\mathbf{v}_g = \frac{\partial \omega_{\lambda}}{\partial \mathbf{q}} \quad (\text{S9})$$

The procedure for calculating lifetimes followed in this work is explained in detail in Ref. [7]. The lifetimes are derived from three-phonon interaction strengths, $\Phi_{\lambda\lambda'\lambda''}$, together with an expression for the conservation of energy. $\Phi_{\lambda\lambda'\lambda''}$ are calculated according to:

$$\begin{aligned} \Phi_{\lambda\lambda'\lambda''} = & \frac{1}{\sqrt{N}} \frac{1}{3!} \sum_{jj'j''} \sum_{\alpha\beta\gamma} W_{\alpha}(j, \lambda) W_{\beta}(j', \lambda') W_{\gamma}(j'', \lambda'') \sqrt{\frac{\hbar}{2m_j \omega_{\lambda}}} \sqrt{\frac{\hbar}{2m_{j'} \omega_{\lambda'}}} \sqrt{\frac{\hbar}{2m_{j''} \omega_{\lambda''}}} \\ & \times \sum_{l'l''} \Phi_{\alpha\beta\gamma}(0j, l'j', l''j'') e^{i\mathbf{q}' \cdot [\mathbf{r}(l'j') - \mathbf{r}(0j)]} e^{i\mathbf{q}'' \cdot [\mathbf{r}(l''j'') - \mathbf{r}(0j)]} e^{i(\mathbf{q} + \mathbf{q}' + \mathbf{q}'') \cdot \mathbf{r}(0j)} \Delta(\mathbf{q} + \mathbf{q}' + \mathbf{q}'') \end{aligned} \quad (\text{S10})$$

As in Eqs. S2/S3, the indices j and l label atoms and unit cells, respectively, and α, β, γ are the Cartesian directions. $\Phi_{\alpha\beta\gamma}$ are the third-order force-constant matrices, ω_{λ} and \mathbf{q} are the phonon frequencies and wavevectors, respectively, W_{α} are the phonon eigenvectors, and $\mathbf{r}(l, j)$ are the atom positions. The function $\Delta(\mathbf{q} + \mathbf{q}' + \mathbf{q}'')$ is unity when the sum of the wavevectors is a reciprocal lattice vector, and zero otherwise, which enforces conservation of momentum. $\Phi_{\lambda\lambda'\lambda''}$ are used to calculate the imaginary part of the self energy, $\Gamma_{\lambda}(\omega)$, using the many-body perturbation theory result (overleaf):

$$\Gamma_\lambda(\omega) = \frac{18\pi}{\hbar^2} \sum_{\lambda'\lambda''} |\phi_{\lambda\lambda'\lambda''}|^2 \{ (n_{\lambda'} + n_{\lambda''} + 1) \delta(\omega - \omega_{\lambda'} - \omega_{\lambda''}) + (n_{\lambda'} - n_{\lambda''}) [\delta(\omega + \omega_{\lambda'} - \omega_{\lambda''}) - \delta(\omega - \omega_{\lambda'} + \omega_{\lambda''})] \} \quad (\text{S11})$$

where n_λ are the phonon occupation numbers, and the delta functions enforce conservation of energy. Assuming three-phonon processes to be the dominant scattering effect, $\Gamma_\lambda(\omega)$ are related to the phonon lifetimes according to:

$$\tau_\lambda = \frac{1}{2\Gamma_\lambda(\omega_\lambda)} \quad (\text{S12})$$

where $2\Gamma_\lambda(\omega_\lambda)$ are the phonon linewidths.

To analyse the thermal transport in more detail, we compared the spread of the (isotropically-averaged) modal contributions to the thermal conductivity, κ_λ , as a function of frequency against the spreads of the group velocity norms, $|\mathbf{v}_{g,\lambda}|$, lifetimes, τ_λ , and average three-phonon interaction strengths, $P_{\mathbf{q}j,\lambda}$ (Figs. S10, 11). Following Ref. [7], $P_{\mathbf{q}j,\lambda}$ are defined here as:

$$P_{\mathbf{q}j,\lambda} = \frac{1}{(3n_a)^2} \sum_{\lambda'\lambda''} |\phi_{\lambda\lambda'\lambda''}|^2 \quad (\text{S13})$$

where n_a is the number of atoms in the unit cell, and $3n_a$ is thus the number of phonon bands at each \mathbf{q} -point.

Figs. S10 and S11 give a breakdown of the modal contributions to the room-temperature thermal conductivity of the *Pnma* and *Cmcm* phases. In the *Pnma* phase, the dominant contribution is clearly from long-lived low-frequency modes, while higher-frequency phonons with larger group velocities account for a secondary contribution. The lifetimes of the low-frequency modes are significantly reduced in the high-temperature phase, and mid-frequency phonons with large group velocities make a proportionately higher contribution to the bulk thermal transport. The latter effect may be due to the soft modes leading to sharp dispersions in the affected bands (c.f. Figs. 1b and 2e in the text). A corresponding analysis of the 800 K thermal conductivity (Figs. S14, S15) shows a very similar pattern, but with a marked reduction in the phonon lifetimes of both phases, particularly of the low-frequency modes.

Finally, we also analysed the contributions of modes with different mean-free paths (MFPs) to the room-temperature thermal conductivity (Fig. S12; the MFP is calculated as $\text{MFP}_\lambda = |\mathbf{v}_{g,\lambda}| \tau_\lambda$). We found that phonons with MFPs below ~ 1 nm make a negligible contribution to the overall heat transport, while the longest phonon MFP observed in either phase was ~ 1 μm . The distribution of cumulative lattice thermal conductivity as a function of increasing phonon MFP is skewed more towards longer paths in the low-temperature *Pnma* phase than in the high-temperature *Cmcm* system, although in both around 50 % of the thermal conductivity is through phonons with MFPs < 10 -20 nm. Again, renormalization of the soft modes in the high-temperature phase makes little difference to the spread of $\kappa_\lambda/\text{MFPs}$, and has a negligible effect on the shape of the thermal-conductivity distribution. At 800 K (Fig. S16), the distributions maintain a similar overall shape, but are skewed towards phonons with shorter MFPs, as would be expected given the reduction in lifetimes evident from comparing Figs. S10/11 and S14/15.

As discussed in the text, these analyses indicate that the comparative reduction in the lifetimes of the low-frequency phonon modes in the *Cmcm* phase is primarily responsible for its lower lattice thermal conductivity. This can

be ascribed to the higher average three-phonon interaction strength experienced by modes in the lower-frequency part of the DoS in the high-temperature phase (Fig. 3 in the text), which belies an inherently higher anharmonicity.

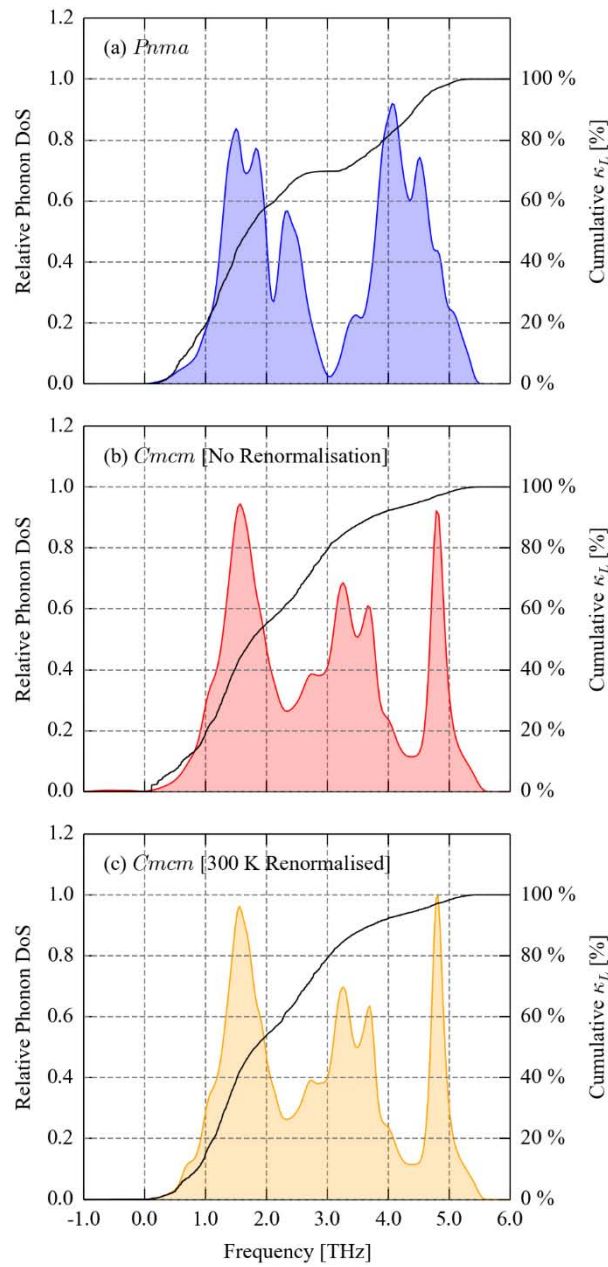


Figure S9 Cumulative average lattice thermal conductivity, κ_L , at 300 K, as a function of phonon frequency, of the *Pnma* (a) and *Cmc̄m* (b, c) phases of SnSe, overlaid on the corresponding phonon density of states curves. The data for the *Cmc̄m* phase in plot (b) is from simulations performed without renormalization of the two soft modes, while the results in plot (c) are obtained with the modes renormalized to the calculated 300 K frequencies ($\tilde{\nu}_1 = 0.971$ and $\tilde{\nu}_2 = 0.659$ THz).

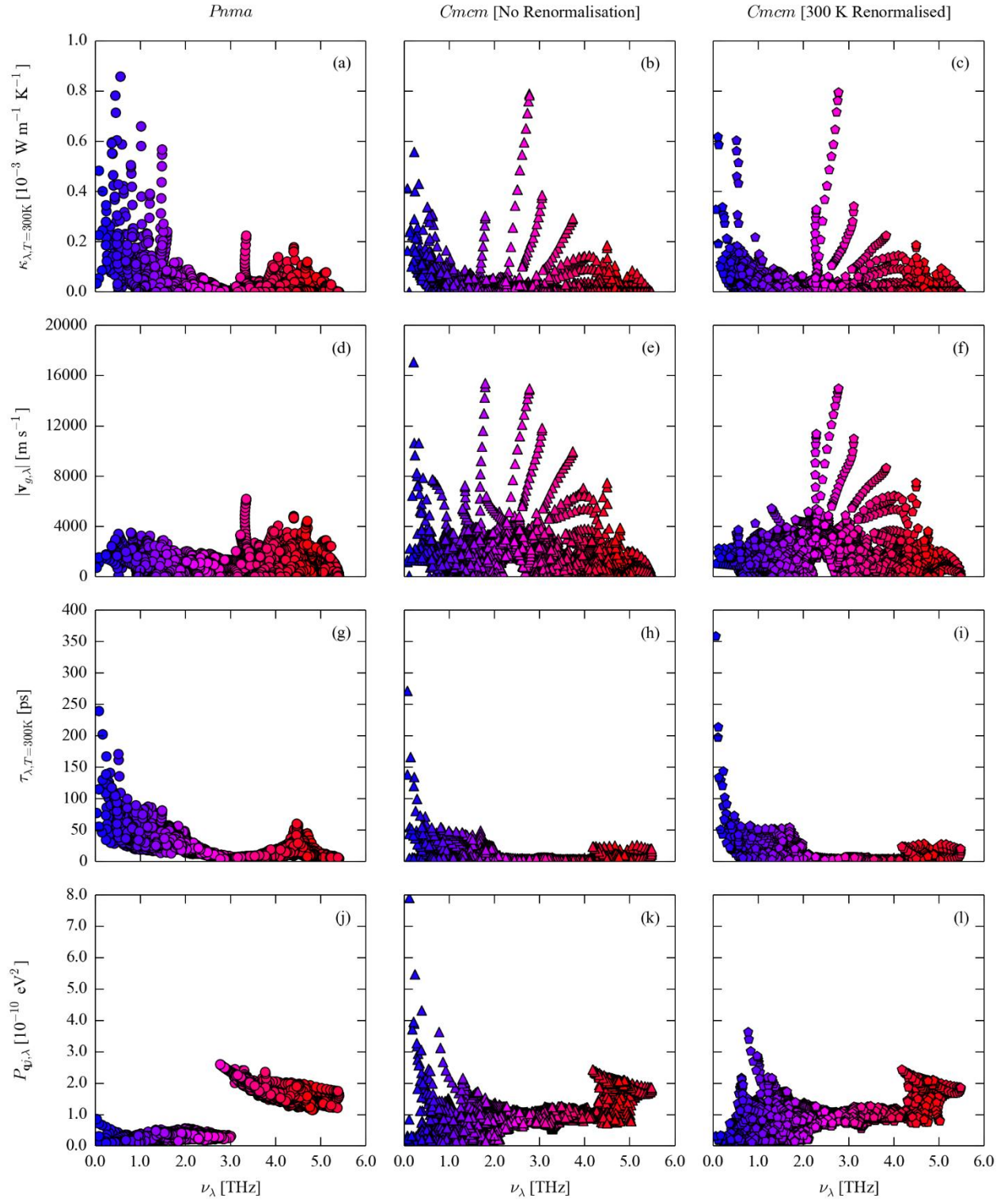


Figure S10 Comparison of the (isotropically-averaged) modal contributions to the lattice thermal conductivity, κ_λ , of SnSe at 300 K (a-c) to the mode group velocities, $|\mathbf{v}_{g,\lambda}|$ (d-f), lifetimes, τ_λ (g-i), and averaged three-phonon interaction strengths, $P_{\mathbf{q}_j,\lambda}$ (j-l; see Eq. S13). The left column shows data for the *Pnma* phase (a, d, g, j), while the other two show data for the *Cmcm* phase without renormalization of the two imaginary modes (center; b, e, h, k) and with the modes renormalized to the calculated 300 K frequencies (right; c, f, i, l; $\tilde{\nu}_1 = 0.971$ and $\tilde{\nu}_2 = 0.659$ THz).

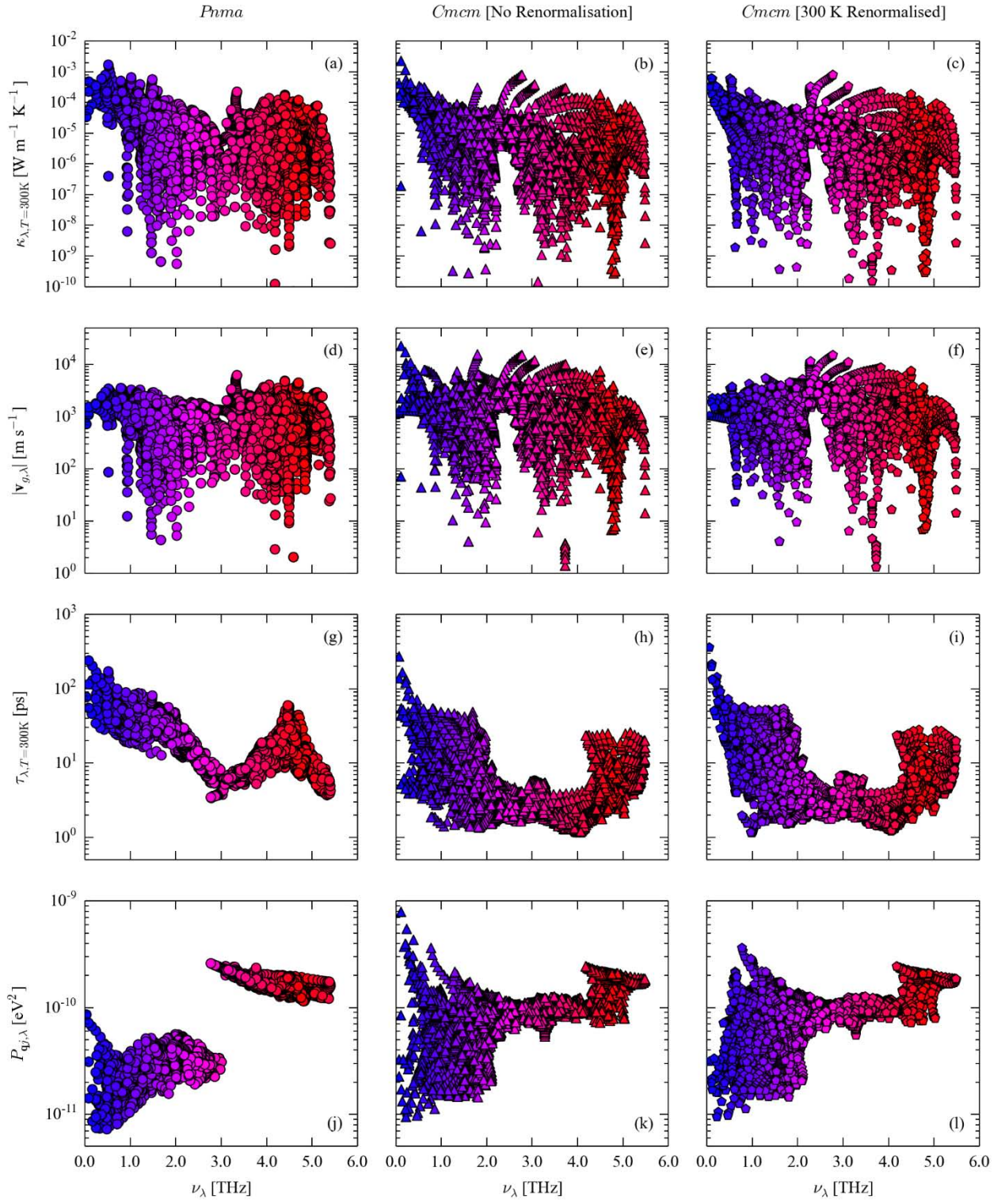


Figure S11 Same data as in Fig. S10, plotted on a logarithmic scale.

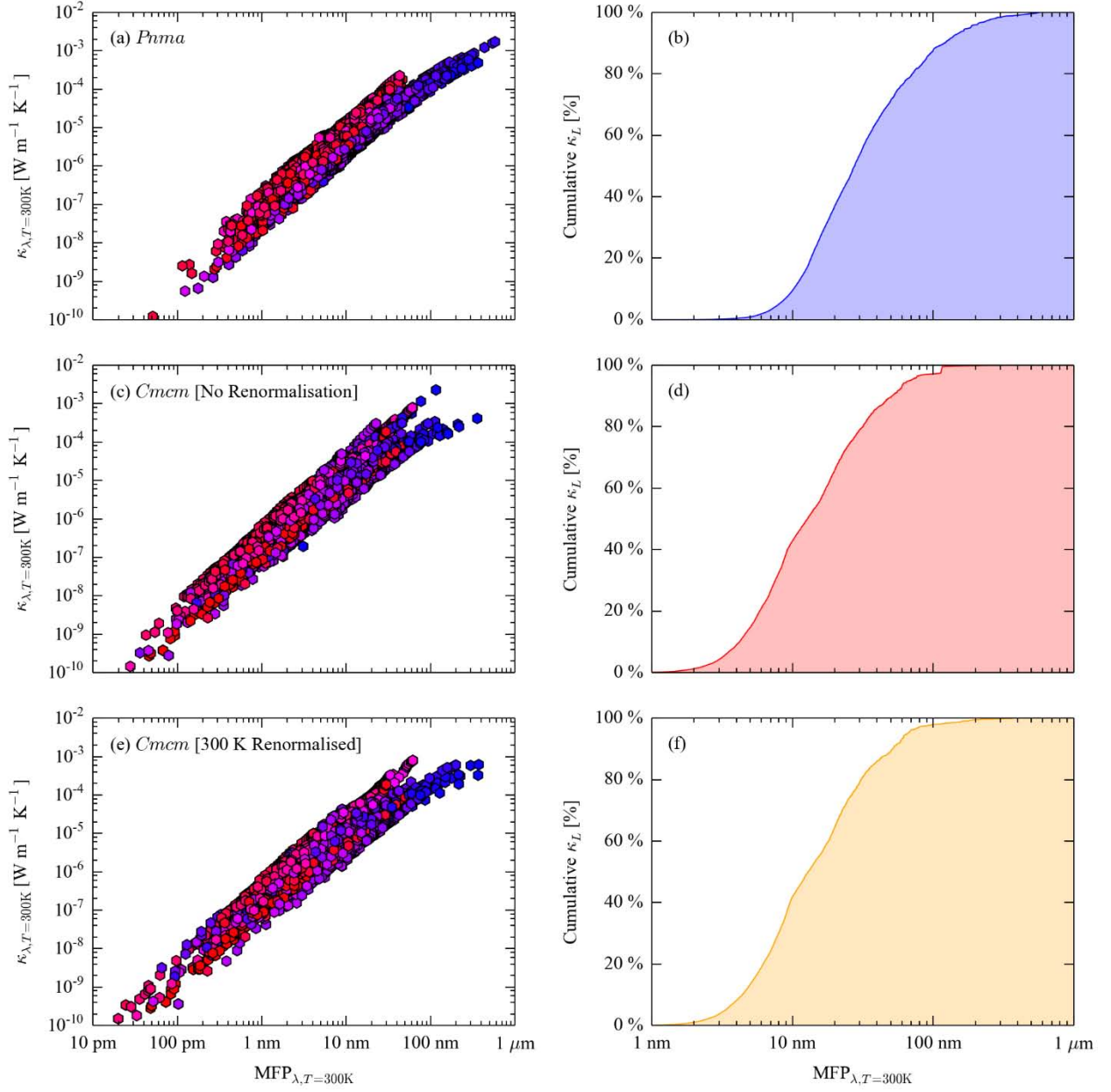


Figure S12 Contributions of modes with different mean-free paths (MFPs) to the average 300 K lattice thermal conductivity (a, c, e), together with the cumulative thermal conductivity over MFPs between 1 nm and 1 μm (b, d, f), for *Pnma* (a, b) and *Cmcm* (c-f) SnSe. For the latter high-temperature phase, two sets of data are shown: one calculated without renormalization of the two soft modes (c, d), and one with the modes renormalized to the calculated effective 300 K frequencies (e, f; $\tilde{\nu}_1 = 0.971$ and $\tilde{\nu}_2 = 0.659$ THz).

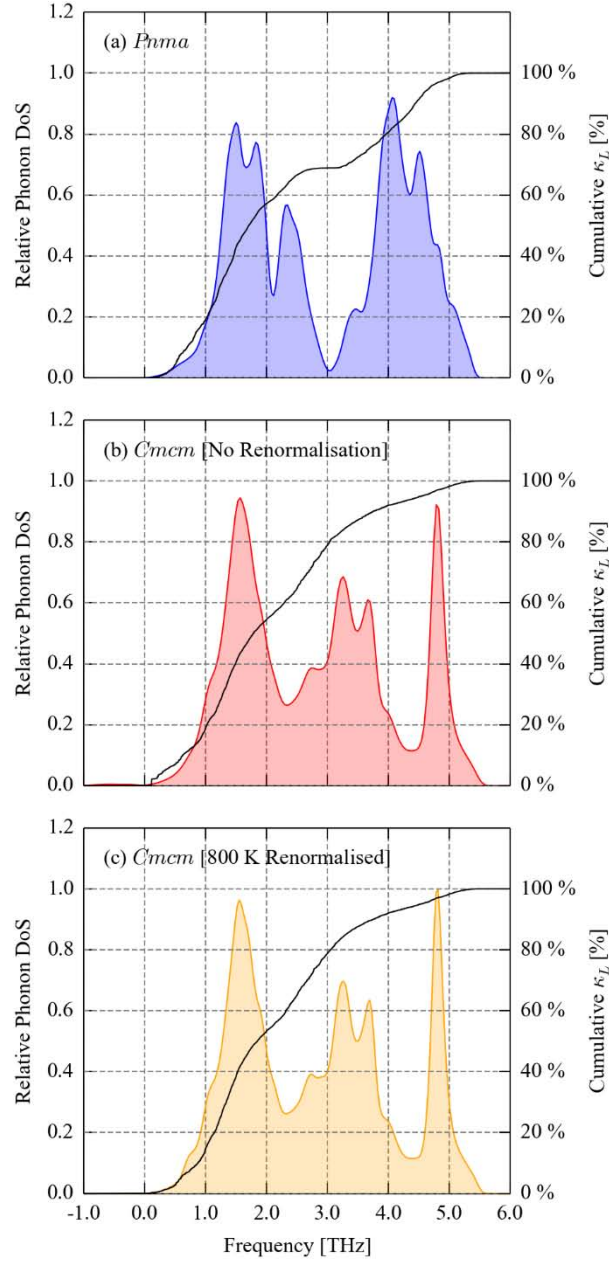


Figure S13 Cumulative average lattice thermal conductivity, κ_L , at 800 K, as a function of phonon frequency, of the *Pnma* (a) and *Cmcm* (b, c) phases of SnSe, overlaid on the corresponding phonon density of states curves. The data for the *Cmcm* phase in plot (b) is from simulations performed without renormalization of the two soft modes, while the results in plot (c) are obtained with the modes renormalized to the calculated 800 K frequencies ($\tilde{\nu}_1 = 1.278$ and $\tilde{\nu}_2 = 0.840$ THz).

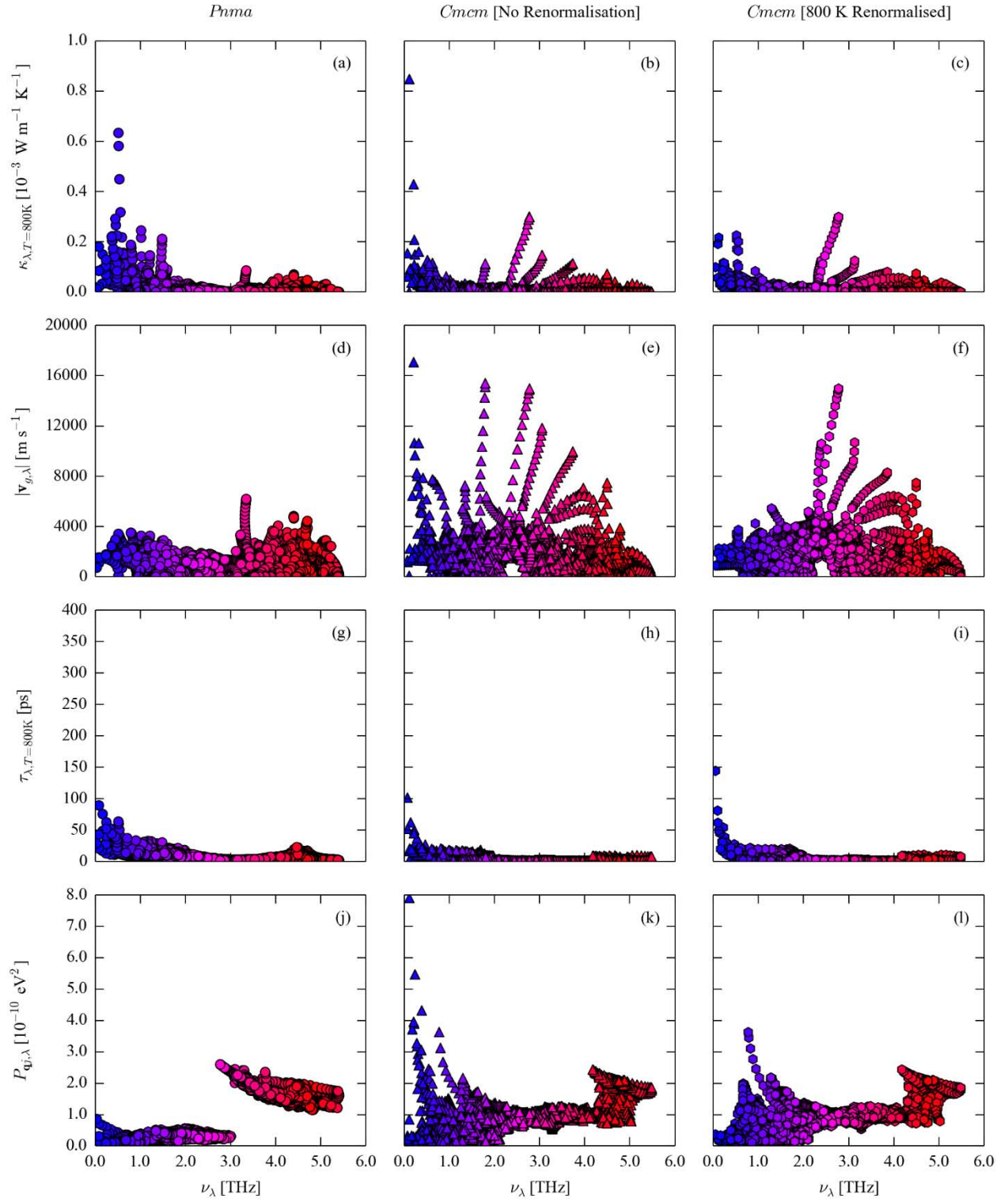


Figure S14 Comparison of the (isotropically-averaged) modal contributions to the lattice thermal conductivity, κ_λ , of SnSe at 800 K (a-c) to the mode group velocities, $|\mathbf{v}_{g,\lambda}|$ (d-f), lifetimes, τ_λ (g-i), and averaged three-phonon interaction strengths, $P_{\mathbf{q}j,\lambda}$ (j-l; see Eq. S13). The left column shows data for the *Pnma* phase (left; a, d, g, j), while the other two show data for the *CmcM* phase without renormalization of the two imaginary modes (center; b, e, h, k) and with the modes renormalized to the calculated 800 K frequencies (right; c, f, i, l; $\tilde{\nu}_1 = 1.278$ and $\tilde{\nu}_2 = 0.840$ THz).

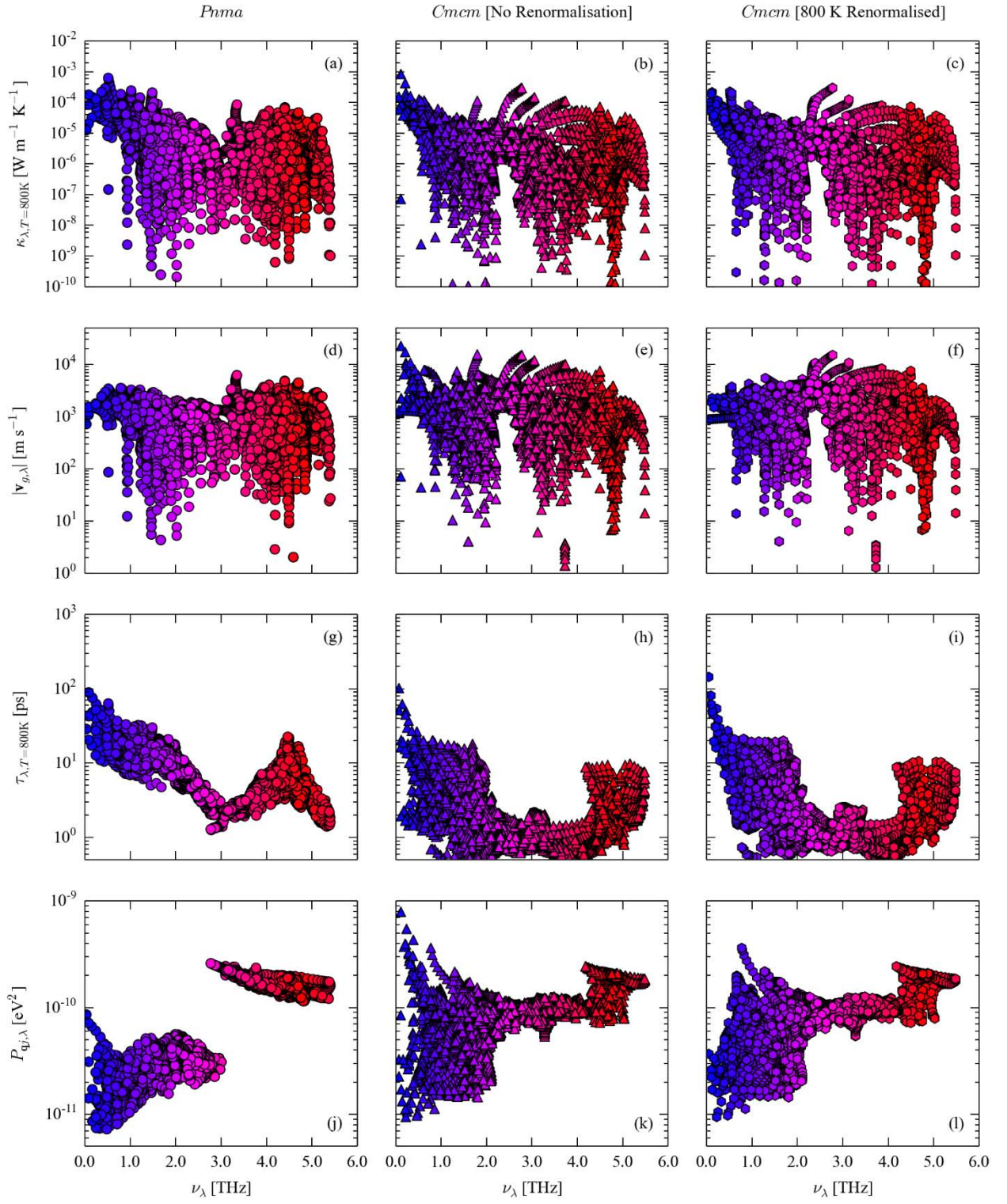


Figure S15 Same data as in Fig. S14, plotted on a logarithmic scale.

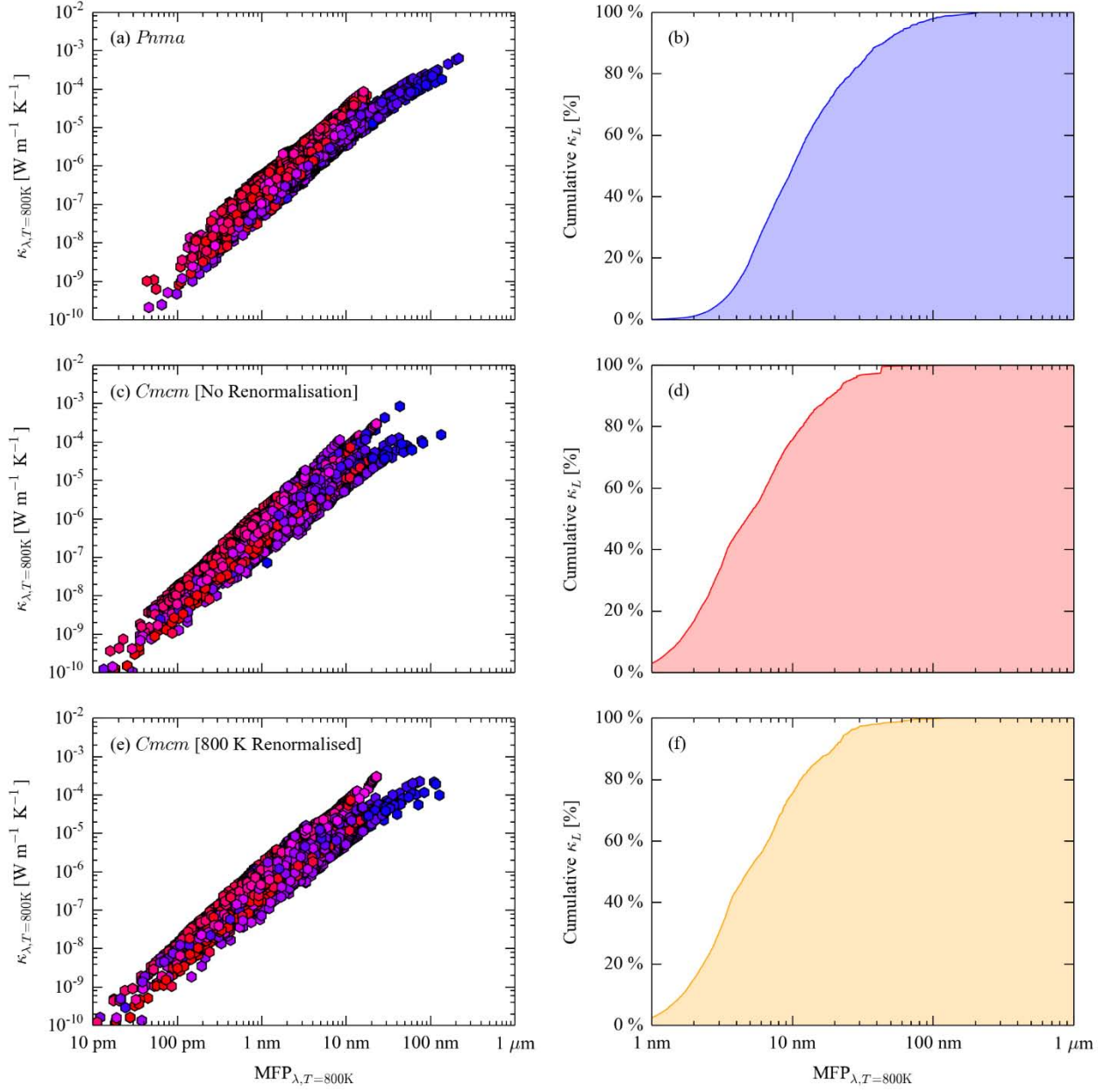


Figure S16 Contributions of modes with different mean-free paths (MFPs) to the average 800 K lattice thermal conductivity (a, c, e), together with the cumulative lattice thermal conductivity over MFPs between 1 nm and 1 μm (b, d, f), for *Pnma* (a, b) and *Cmc̄m* (c-f) SnSe. For the latter high-temperature phase, two sets of data are shown: the first is calculated without renormalization of the two soft modes (c, d), and the other with the modes renormalized to the calculated effective 800 K frequencies (e, f; $\tilde{\nu}_1 = 1.278$ and $\tilde{\nu}_2 = 0.840$ THz).

9. References

- [1] G. Kresse and J. Hafner, Physical Review B **47** (1993).
- [2] P. E. Blochl, Physical Review B **50**, 17953 (1994).
- [3] G. Kresse and D. Joubert, Physical Review B **59** (1999).
- [4] J. P. Perdew, A. Ruzsinszky, G. I. Csonka, O. A. Vydrov, G. E. Scuseria, L. A. Constantin, X. L. Zhou, and K. Burke, Physical Review Letters **100** (2008).
- [5] H. J. Monkhorst and J. D. Pack, Physical Review B **13**, 5188 (1976).
- [6] A. Togo, F. Oba, and I. Tanaka, Physical Review B **78**, 134106 (2008).
- [7] A. Togo, L. Chaput, and I. Tanaka, Physical Review B **91**, 094306 (2015).
- [8] K. Parlinski, Z. Q. Li, and Y. Kawazoe, Physical Review Letters **78**, 4063 (1997).
- [9] K. Momma and F. Izumi, J Appl Crystallogr **44**, 1272 (2011).
- [10] B. S. Garbow, Comput Phys Commun **7**, 179 (1974).
- [11] J. Buckeridge and S. Fahy, Physical Review B **84**, 144120 (2011).